American Mineralogist, Volume 106, pages 374–388, 2021

Competitive adsorption geometries for the arsenate As(V) and phosphate P(V) oxyanions on magnetite surfaces: Experiments and theory

Xiaoliang Liang[1,2,7], Xiaoju Lin[1,2,7], Gaoling Wei[3,4], Lingya Ma[1,2,7], Hongping He[1,2,7,*], David Santos-Carballal[5,*], Jianxi Zhu[1,2,7], Runliang Zhu[1,2,7], and Nora H. De Leeuw[5,6]

[1]CAS Key Laboratory of Mineralogy and Metallogeny/Guangdong Provincial Key Laboratory of Mineral Physics and Material Research and Development, Guangzhou Institute of Geochemistry, Chinese Academy of Sciences, Guangzhou 510640, P.R. China
[2]CAS Center for Excellence in Deep Earth Science, Guangzhou, 510640, China
[3]Guangdong Key Laboratory of Integrated Agro-environmental Pollution Control and Management, Guangdong Institute of Eco-environmental Science and Technology, Guangzhou 510650, China
[4]National-Regional Joint Engineering Research Center for Soil Pollution Control and Remediation in South China, Guangzhou 510650, China
[5]School of Chemistry, University of Leeds, Leeds LS2 9JT, U.K.
[6]Department of Earth Sciences, Utrecht University, Princetonplein 8A, 3584 CD Utrecht, The Netherlands
[7]University of Chinese Academy of Sciences, Beijing 100049, P.R. China

Abstract

In the present study, the competitive adsorption geometries for arsenate and phosphate on magnetite surfaces over a pH range of 4–9 were investigated using in situ attenuated total reflectance Fourier-transform infrared spectroscopy (ATR-FTIR) and two-dimensional correlation analysis (2D-COS). The adsorption energies and infrared vibrational frequencies of these surface complexes were also calculated by first-principles simulations. Arsenate and phosphate have different preferences for the magnetite surface in the presence of aqueous solvent at both acid and alkaline pH. For the adsorption of phosphate, mono-protonated monodentate mononuclear (MMM) complexes dominated at acid pH, while non-protonated bidentate binuclear (NBB) complexes were dominant at alkaline pH. Arsenate mainly formed bidentate binuclear (BB) complexes with some outer-sphere species, both of which were more prevalent at acid pH. The pre-absorbed inner-sphere arsenate species were scarcely affected by the introduction of phosphate. However, the pre-absorbed phosphate oxyanions, especially the MMM complexes, were significantly substituted by BB arsenate at the magnetite surfaces. The adsorption affinity of phosphate and arsenate species for magnetite surface was found to increase in the following order: MMM phosphate complex < NBB phosphate complex < BB arsenate complex, which was consistent with the calculated adsorption energies. The simulated infrared vibrational frequencies for the most favorable adsorption modes of each oxyanion display distinctive patterns, and their trends are in excellent agreement with experimental data.

The effects of pH, adsorption sequence, and mineral species on the competitive adsorption between arsenate and phosphate oxyanions are also discussed, and their different competing ability and stability on the magnetite surfaces can be ascribed to the variations in adsorption geometry and strength of binding. To the best of our knowledge, this is the first study aiming to distinguish the stability of the different phosphate and arsenate complexes on magnetite by employing a combined approach of in situ spectroscopy and DFT simulations. Our results provide molecular-level insight into the geometries and relative stabilities of the adsorption of phosphate and arsenate on magnetite surfaces, which is useful for interpretation of the mobility and bioavailability of these anions.

Keywords: Phosphate, arsenate, competitive adsorption, adsorption geometry, ATR-FTIR, first-principles simulations

Introduction

Contamination of soil and aquatic systems by arsenic (As) and phosphorus (P) is of global environmental concern. Arsenic is often found at elevated concentrations in freshwater, attributed to various natural (e.g., geothermal processes and mineral weathering) and anthropogenic (e.g., mining industry and agriculture) processes (Kocourkova-Vikova et al. 2015; Kunhikrishnan et al. 2017). Owing to its biotoxicity and carcinogenic risks, the presence of arsenic in drinking water ranks among the greatest threats to public health (Antelo et al. 2015), which has led the World Health Organization (WHO) to propose a limit of 10 μg L^{-1} (WHO 2011). However, in the arsenic-contaminated water, the As concentration can reach several parts per million (Chakraborti et al. 2002; Sprague and Vermaire 2018; Winkel et al. 2011). Arsenic exists in several oxidation states (–III, 0, III, and V),

* E-mail: hehp@gig.ac.cn and D.Santos-Carballal@leeds.ac.uk

0003-004X/21/0003–374$05.00/DOI: https://doi.org/10.2138/am-2020-7350

with arsenate (AsO_4^{3-}) being the most common form found in natural aqueous systems (Choppala et al. 2016). Phosphorous (P) is an essential nutrient for plant growth. But the input of excess P from agricultural land runoff or over-fertilization may lead to levels above the limit of 0.1 mg L^{-1} recommended by the U.S. Environmental Protection Agency (USEPA), causing severe environmental problems including eutrophication (Neupane et al. 2014). P occurs naturally only in the pentavalent state, forming ortho-phosphates, pyrophosphates, longer-chain polyphosphates, and several types of organic phosphates (Correll 1998).

After their release from natural and anthropogenic sources, As and P undergo a series of geochemical reactions, e.g., adsorption, reduction/oxidation, precipitation (Zhang et al. 2017b), and sequestration by soil and sediments (Grossl et al. 1997). The adsorption at the mineral/water interface is vital for their mobility. Iron (hydr)oxides are ubiquitous in soils and aquatic sediments (Pedersen et al. 2005), with high adsorption affinity toward arsenate and phosphate. The surface complexation is the dominant adsorption mechanism reported for arsenate and phosphate species, as verified in macroscopic batch experiments (Swedlund et al. 2014), model calculations (Tiberg et al. 2013), and microscopic studies (Johnston and Chrysochoou 2014). Bidentate-binuclear (BB), monodentate-mononuclear (MM), and bidentate-mononuclear (BM) complexes are the prevalent surface-binding configurations of arsenate and phosphate on iron oxides (Fendorf et al. 1997; Liu et al. 2015), with distribution dependent on pH, ionic strength, and surface coverage (Krumina et al. 2016). Generally, the ability to form bridging bidentate surface complexes depends upon the proximity of terminal Fe-O sites on the surface (Livi et al. 2017; Villalobos et al. 2009).

P and As belong to group 5A of the periodic table and form species with comparable chemical properties. Both arsenate and phosphate oxyanions have a tetrahedral geometry with close thermochemical radii, i.e., 2.48 and 2.38 Å (da Silva and Williams 2001), respectively, and very similar proton affinities, e.g., 2.2, 7.0, and 11.5 for pKa_1, pKa_2, and pKa_3 of arsenate and 2.2, 7.2, and 12.3 for pKa_1, pKa_2, and pKa_3 of phosphate, respectively (Elzinga and Sparks 2007; Mohan and Pittman 2007). Thus, they display analogous adsorption characteristics in the aspects of kinetics, pH dependence, and effect of ionic strength. As arsenate and phosphate oxyanions frequently occur together in surface environments, their competitive adsorption onto mineral surfaces explicitly determines their bioavailability and leachability, which is crucial for the prediction of potential risk of environmental contamination. However, the current knowledge on this hypothesis is scattered and fragmented, even regarding the adverse effect of phosphate on arsenate adsorption. For example, arsenate is found preferentially adsorbed on iron oxide at a low pH, whereas phosphate shows the opposite trend (Han and Ro 2018). But in soil stabilized by iron oxide, phosphate can replace the adsorbed arsenate when the concentration of the former is larger than the latter (So et al. 2012). This is contrary to the results reported by Hashem et al. (2015), where arsenate was found bonded to iron oxide more strongly than phosphate (Hashem et al. 2015). Moreover, contradictory information is also found in the literature concerning the adsorption geometry. For arsenate, BB complexes were considered as the predominant adsorption configuration on iron oxide surfaces (Carabante et al. 2010). MM coordination is also found for arsenate binding on some iron oxides, as verified by combined EXAFS and IR analyses (Antelo et al. 2015; Loring et al. 2009). Although BM configuration has also been assigned under certain conditions (Neupane et al. 2014), these have been excluded by Sherman and Randall (2003) as the EXAFS signal attributed to the BM complex was simply due to multiple scattering. For phosphate, the IR analysis indicates that protonated BB complexes are the predominant species on iron oxides at pH between 3 and 6, whereas the non-protonated BB complexes are dominant at pH > 7.5 (Carabante et al. 2010). On the contrary, the surface complexation modeling (SCM) predicts that deprotonated BB phosphate and deprotonated MM phosphate dominate at lower-pH and higher-pH values, respectively, while the contribution of protonated BB is very small (Kanematsu et al. 2010). This shows that great divergence in the competitiveness exists not only within the individual adsorption geometries of phosphate and arsenate, but also during their co-adsorption.

To date, the competitive adsorption of arsenate and phosphate on calcite (So et al. 2012), clay minerals (Violante and Pigna 2002), and certain iron oxides, e.g., ferrihydrite (Antelo et al. 2015) and goethite (Zhao and Stanforth 2001), has been investigated intensively. In comparison, their competitive adsorption on magnetite, which is a common constituent of soil and sediment, is poorly understood. Magnetite exists in anoxic sediments and soils (Guo and Barnard 2013), and it is formed naturally via several pathways, including ferrous iron oxidation and iron metal corrosion, as well as chemical and biological reduction of ferric oxides (Gorski et al. 2010). Additionally, the remediation of contaminated groundwater and soil is increasingly carried out using an emerging technology based on zero-valent iron (ZVI) nanoparticles, where magnetite is the major corrosion product formed as the outer layer of ZVI (Filip et al. 2014). With the inverse spinel structure, magnetite has several features that make its reaction properties interesting, specifically: (1) electron donor Fe^{2+} ions on octahedral sites, which are active for the reduction of certain oxyanions, e.g., CrO_4^{2-} and UO_3^-; and (2) octahedral Fe^{2+} and Fe^{3+} cations, which can oxidize and reduce reversibly during the reaction with adsorbed oxyanions, while keeping the spinel structure unaffected. In previous studies, magnetite is shown to be efficient at scavenging metal oxyanions in natural and engineered aquatic systems, including chromate (Zhang et al. 2017a), arsenate (Zhang et al. 2011), and uranyl (Scott et al. 2005). These properties and behavior highlight the important role of magnetite in the transport of arsenate and phosphate in soil and aqueous systems. Due to the low specific surface area or surface site density of magnetite (<50 m^2 g^{-1}, 1–2 sites nm^{-2}) (Sun et al. 1998; Tamura et al. 1993), relative to ferrihydrite (>200 m^2 g^{-1}, 2.5–3 sites nm^{-2}) (Hiemstra 2013) and goethite (<50 m^2 g^{-1}, 2.5–3.5 sites nm^{-2}) (Ona-Nguema et al. 2005; Zhao and Stanforth 2001), the resulting low surface coverage of arsenate and phosphate on magnetite makes it difficult to analyze spectroscopically. Extended X-ray absorption fine structure (EXAFS) spectroscopy is the most widespread technique used to investigate the geometry of surface complexes (Ona-Nguema et al. 2005), which has shown the formation of BB arsenate complexes on the surfaces of ferrihydrite,

hematite, goethite, and lepidocrocite (Sherman and Randall 2003). However, it is difficult to analyze light elements such as P using soft X-rays, due to their poor signal-to-noise ratios. In situ attenuated total reflectance Fourier-transform infrared (ATR-FTIR) spectroscopy is a reliable method that is capable of tracing the coordination environment and protonation state of most oxyanions at mineral-water interfaces without the interference of signals from the liquid phase (Brechbuhl et al. 2012). Although the individual and competitive coordination structure of phosphate and arsenate on ferrihydrite, goethite, and hematite has been previously investigated using ATR-FTIR, the analysis of the relatively broad vibrational bands has led to inconclusive interpretation (Gao et al. 2013). Recently, two-dimensional correlation spectroscopy (2D-COS) has been successfully applied in ATR-FTIR analysis by resolving overlapped peaks and enhancing the spectral resolution (Yan et al. 2016). Despite the advances achieved using ATR-FTIR in the understanding of the adsorption mechanism and geometries of phosphate and arsenate complexes, it is still unclear what are the factors that drive their competition under complex and realistic conditions. This uncertainty may be resolved by employing periodic density functional theory (DFT) calculations and comparing the simulated geometries, vibrational modes, and/or relative adsorption energies to experimental results, which will provide a better understanding from a thermodynamic point of view of the competition between arsenate and phosphate (He et al. 2009).

In this study, the competitive adsorption of arsenate and phosphate species on the surface of chromium-doped magnetite was investigated by in situ ATR-FTIR spectroscopy and complemented by DFT calculations. An interesting feature of natural magnetite is the substitution of iron by other metals while maintaining the spinel structure. Cr is a common impurity element in natural magnetite as trace element (<0.1%), minor element (0.1–1%), and major element (more than 1%), forming solid-solution series between magnetite (Fe_3O_4) and chromite ($FeCr_2O_4$) (Dupuis and Beaudoin 2011). Moreover, the substitution of Cr^{3+} for Fe^{3+} is known to enhance the adsorption capacity of magnetite (Liang et al. 2012), and thus increase the signals and accuracy of in situ ATR-FTIR experiments. The competitive adsorption was carried out under different addition subsequences. A comparison between our results and previous investigations was also conducted and a comprehensive atomic-level understanding on the adsorption of phosphate and arsenate on magnetite is used to better interpret their geochemical behaviors on the Earth surface and their effects on nucleation, growth, and phase transformation of the mineral phases.

Materials and methods

Preparation of Cr-substituted magnetite

Magnetite with Cr substitution was synthesized by the precipitation-oxidation method described in Online Material[1] OM1. The obtained sample had the spinel structure (Online Material[1] Figure OM1) and the X-ray absorption fine structure (XAFS) spectra indicated that chromium in the valence state of +3 mainly occupied the octahedral sites. The detailed discussion of XAFS results has been presented elsewhere (Liang et al. 2013). The high surface area (112 $m^2\ g^{-1}$) and surface site density (3.6 sites nm^{-2}) of the magnetite particles (Online Material[1] Table OM1) increased the likelihood of obtaining good contact and allowed us to probe large quantities of adsorbed species (Liang et al. 2017). During the adsorption, the concentration of leaching Cr and Fe was below the detection limit of the instrument.

In situ ATR-FTIR and 2D-COS analyses

In situ ATR-FTIR analysis of phosphate and arsenate adsorption on magnetite was conducted using a Bruker Vertex 70 FTIR spectrometer equipped with a liquid N_2-cooled MCT detector and a horizontal ATR accessory made of ZnSe crystal. Before the IR analysis, the magnetite particle layer was prepared on a ZnSe crystal. 1 mL of magnetite suspension (5 g L^{-1}) was dropped onto the crystal surface and dried overnight at room temperature. The film was then rinsed with deionized (DI) water to remove the loosely deposited particles, which stabilized the deposited layer (Hug 1997). At the end of adsorption experiment, the magnetite film was inspected for signs of film erosion, which were not observed.

Before adsorption, a NaCl background electrolyte solution (0.01 mol L^{-1}) at the designated pH was flowed through the cell with magnetite deposition layer at a rate of 1 mL min^{-1} until no further change in spectra was seen. A background spectrum comprising the absorbance of the ZnSe crystal and the deposited adsorbent was then collected, followed by the injection of solutions containing 100 μmol L^{-1} of arsenate or phosphate, and 0.01 mol L^{-1} of NaCl to start the adsorption reaction. IR spectra were recorded as a function of time until the adsorption reached equilibrium without any signal variation. NaCl was selected as the background electrolyte, because it was inert or not adsorbed on solid surfaces. All liquid samples were purged with N_2 during spectrum collection. The pH was adjusted within the range of 4.0–9.0 using NaOH (0.1 mol L^{-1}) and HCl (0.1 mol L^{-1}). Desorption experiments were conducted by introducing NaCl solution (0.01 mol L^{-1}) into the ZnSe cell when the adsorption of oxyanions reached equilibrium. The comparative adsorption was carried out through the reversible substitution of arsenate solution (100 μmol L^{-1} at pH 4.0 and 7.0, and 500 μmol L^{-1} at pH 9.0) with phosphate solution of the same concentration. It is necessary to emphasize that the arsenate concentrations used in this study, i.e., 100 and 500 ppm are at the low end of the range of concentrations examined in past experimental studies (molecular-scale studies: 5 to 10000 μmol L^{-1}, macroscopic studies: 0.7 to 30000 μmol L^{-1}), as indicated by Catalano et al. (2008).

The IR spectra were processed and analyzed with the OPUS software. Curve-fitting analysis of the peaks was conducted using the Gaussian line shape. To obtain an accurate assignment of the IR peaks for the surface complexes, the spectra were analyzed using the 2D-COS technique (Online Material[1] OM2).

Computational methods

To simulate the interaction between the Fe_3O_4(001) surface and phosphate/arsenate oxyanions in aqueous solution, the periodic plane-wave density functional theory (DFT) method within the Vienna ab initio simulation package (VASP) was employed (Kresse and Furthmuller 1996a,1996b; Kresse and Hafner 1993, 1994). The Perdew, Burke, and Ernzerhof (PBE) semi-local functional approximation was used to calculate the exchange-correlation energy (Perdew et al. 1996, 1997). The projector augmented wave (PAW) method was used to model the atomic frozen core states and their interaction with the valence levels (Fe: 4*d*5*s*, O: 2*s*2*p*, H: 1*s*, P: 3*s*3*p* and As: 4*s*4*p*) (Blochl 1994; Kresse and Joubert 1999). The expansion of the Kohn-Sham (KS) valence states was calculated with a kinetic energy cut-off of 400 eV. We have tested larger cut-off values, but these led to negligible energy differences with respect to a reference, such as the adsorption energies reported in our previous studies (Santos-Carballal et al. 2014, 2018). The electronic partial occupancies were determined during geometry optimizations using the Gaussian smearing method with the width set at 0.02 eV (Mermin 1965). Furthermore, the tetrahedron method with Blöchl corrections was used in static simulations to obtain accurate total energies as well as all the electronic and magnetic properties. Long-range dispersion interactions were modeled using the D2 semi-empirical method of Grimme (2006). The optimization of the structures was conducted via the conjugate-gradients method, which stopped when the forces on all atoms were smaller than 0.01 eV·$Å^{-1}$. The Dudarev et al. (1998) approach was used within the DFT+*U* methodology (Anisimov et al. 1992) to improve the description of the localized and strongly correlated Fe *d* states, which were corrected by applying the value of U_{eff} = 3.7 eV (Santos-Carballal et al. 2014, 2018). All calculations were spin-polarized and the initial magnetic moments were set following a high-spin ferrimagnetic structure, i.e., with opposite spins in the tetrahedral and octahedral sites (Néel 1948; Shull et al. 1951). These criteria allowed convergence of the total electronic energy within 10^{-4} eV per atom. We decided to only model the magnetite (001) surface as this is the thermodynamically most stable facet, with the lowest relaxed surface energy and the most prominent plane in the calculated crystal morphology (Santos-Carballal et al. 2014), which is in agreement with the observations made by Zhao et al. (2008) at pH ≤ 13. Moreover, Jönsson and Sherman (2008) found that the bidentate interaction of the inner-sphere As(V) complexes is only possible at the rows of exposed Fe_B ions formed in the [011]

direction of the magnetite (001) surface, which is in line with its largest density of exposed Fe cations (Santos-Carballal et al. 2014). However, similar to goethite, we cannot rule out that arsenate and phosphate may have different affinities for other less stable and less prominent magnetite surfaces, which may saturate with a small fraction of the total number of adsorbed oxyanions (Kubicki et al. 2012), thus providing a minor contribution to the observed infrared spectra. For the inner-sphere complexes, the adsorption of the phosphate and arsenate species on the Fe_3O_4(001) surface was simulated under both acid and alkaline conditions. Different initial binding geometries, including MM, BM, BB, and tridentate trinuclear (TT), were taken into account. All possible binding sites were also inspected, including the protruding Fe_A atom and the Fe_B ion as well as their possible combinations. Thus, we are confident that we have considered all possible adsorption geometries for the oxyanion complexes. However, given the large positional degree of freedom of the water molecules, there may be some uncertainty in their location, but this lies beyond the scope of this work. Further details of the computational methods used, including surface models, inner- and outer-sphere complex models, the approach used for the simulation of acid and alkaline conditions, calculation of adsorption energy, Bader charges and vibrational frequencies are presented in Online Material[1] OM3 and Online Material[1] Figure OM2.

Results and discussion

Individual molecular adsorption

Arsenate adsorption on magnetite. The intensity of characteristic bands obtained by in situ ATR-FTIR was proportional to the level of adsorption; as pH decreased, the arsenate adsorption was obviously enhanced (Online Material[1] Figure OM3). Given the point of zero charge (PZC) of magnetite at 6.8 (Online Material[1] Table OM1), the surface of this mineral gradually changed from negative charge at alkaline pH to positive charge under acid conditions, improving the adsorption of arsenate oxyanions. Besides band intensity, the spectrum profile also showed significant changes with pH. At high pH, the spectra displayed a broad but asymmetrical band at 855 cm^{-1}, with a shoulder peak at 820 cm^{-1}. As the pH decreases, the band at 855 cm^{-1} became more symmetrical and sharpened, which was also characteristic of aqueous $HAsO_4^{2-}$ (Online Material[1] Figure OM4). Thus, outer-sphere (OS) $HAsO_4^{2-}$ complexes were formed on magnetite at acidic pH, which was verified in desorption experiments at pH = 4.0 (Online Material[1] Figure OM5). Once the arsenate solution was replaced by NaCl solution, the intensity of the band at 855 cm^{-1} quickly decreased in 10 min, and then slowly declined in the following 140 min, suggesting the coexistence of both OS and inner-sphere (IS) arsenate complexes, as OS species have faster desorption rates than IS species (Catalano et al. 2008). According to previous work, neither As(III) oxidation nor As(V) reduction occurs on the magnetite surface (Jonsson and Sherman 2008).

According to the 2D-COS analysis results (Online Material[1] OM5), the band at 855 cm^{-1} and those at 870, 830, and 805 cm^{-1} are attributed to different adsorption complexes of arsenate. The band at 855 cm^{-1} was identical to that of aqueous $HAsO_4^{2-}$ (Online Material[1] Figure OM4), supporting the formation of these OS complexes. The contribution at 870 cm^{-1} was assigned to the asymmetric stretching (ν_3) of As-O, while those at 830 and 805 cm^{-1} were assigned to the asymmetric and symmetric stretchings (ν_3) of As-OFe, respectively (Brechbuhl et al. 2012; Hu et al. 2015). The presence of three ν_3 bands indicated the C_2v or lower symmetry for the IS arsenate complexes. The above characteristic bands are consistent with the observations of arsenate adsorption on ferrihydrite, hematite, and rutile (Brechbuhl et al. 2012; Hu et al. 2015). Gao et al. attributed the IR bands at 830 and 804 cm^{-1} to the arsenate adsorbed in the BB geometry on the ferrihydrite surfaces at high pH (Gao et al. 2013). The BB complexes are also the dominant geometry of arsenate adsorbed on most iron (hydr)oxides, as verified by EXAFS (Jonsson and Sherman 2008; Sherman and Randall 2003). Thus, in this study, the IS arsenate complexes on magnetite were also assigned to the BB geometry.

The ATR-FTIR spectra were deconvoluted to gain additional insight into the arsenate adsorption geometries (Fig. 1a). The relative amounts of adsorbed OS and IS species and their contributions to the total adsorption (based on the sub-spectral area) varied with pH (Fig. 2a). At pH > 7, almost no OS complexes were formed, ascribed to the electrostatic repulsive force between the arsenate oxyanions and the negatively charged magnetite surface. The IS complexes with BB geometry are the main species at high pH (Eq. 1). As the pH decreased, the magnetite surface became positively charged, leading to the rapid increase in both the adsorption and contribution of OS complexes (Eq. 2). Once the OS complexes were formed, the Coulombic attraction between the magnetite surface and arsenate oxyanions further improved the formation of IS complexes with BB geometry by ligand exchange. These findings explain why the IS species dominate over the OS complexes throughout the studied pH range.

$$2{\equiv}FeOH + HAsO_4^{2-} \rightarrow ({\equiv}FeO)_2(AsO)OH + 2OH^- \quad (1)$$

$${\equiv}FeOH_2^+ + H_2AsO_4^- \rightarrow {\equiv}FeOH_2^+\cdots HAsO_4^{2-} + H^+ \quad (2)$$

Phosphate adsorption on magnetite. The adsorption of phosphate on magnetite was also affected by pH (Online Material[1] Figure OM7). When pH decreased from 9.0 to 4.0, the IR spectra increased in intensity and displayed variations in shape. Specifically, a blue-shift of the highest peak from 1028 cm^{-1} (pH = 9.0) to 1050 cm^{-1} (pH = 4.0) was seen, alongside the appearance of two shoulder peaks at 1000 and 1100 cm^{-1}. The IR spectra of the adsorbed phosphate were clearly different from the aqueous phosphate oxyanions at identical pH (Online Material[1] Figure OM8), suggesting the formation of IS complexes. This is also confirmed in the desorption experiment at pH = 4.0 (Online Material[1] Figure OM9), where the IR intensity only decreased slightly after desorption for 180 min.

Based on the 2D-COS analysis (Online Material[1] OM5), the IR bands of phosphate at 1075, 1028, and 965 cm^{-1} and those at 1108, 1050, 1000, and 870 cm^{-1} were assigned to different IS complexes of phosphate. Both complexes had three ν_3 vibrations, indicating a C_2v symmetry or lower. Through the deconvolution of the spectra (Fig. 1b) and the calculation of their sub-spectral areas (Fig. 2b), the contribution of each predominant adsorbed phosphate complex was calculated at acid and alkaline pH (Fig. 2b). Based on the very close IR signals at high pH, a complex with similar coordination environment and protonation degree to 1075, 1028, and 965 cm^{-1} was reported for the adsorption of phosphate onto ferrihydrite (1070, 1025, and 940 cm^{-1}) (Arai and Sparks 2001; Carabante et al. 2010). These complexes were in a non-protonated form, as confirmed through the comparison of spectra obtained in D_2O and H_2O medium (Arai and Sparks 2001). Considering their C_2v or C_1 symmetry and the alkaline pH range of stability, these non-protonated species were affiliated to BB complexes (Eq. 3) (Arai and Sparks 2001; Kubicki et al. 2012), which were also

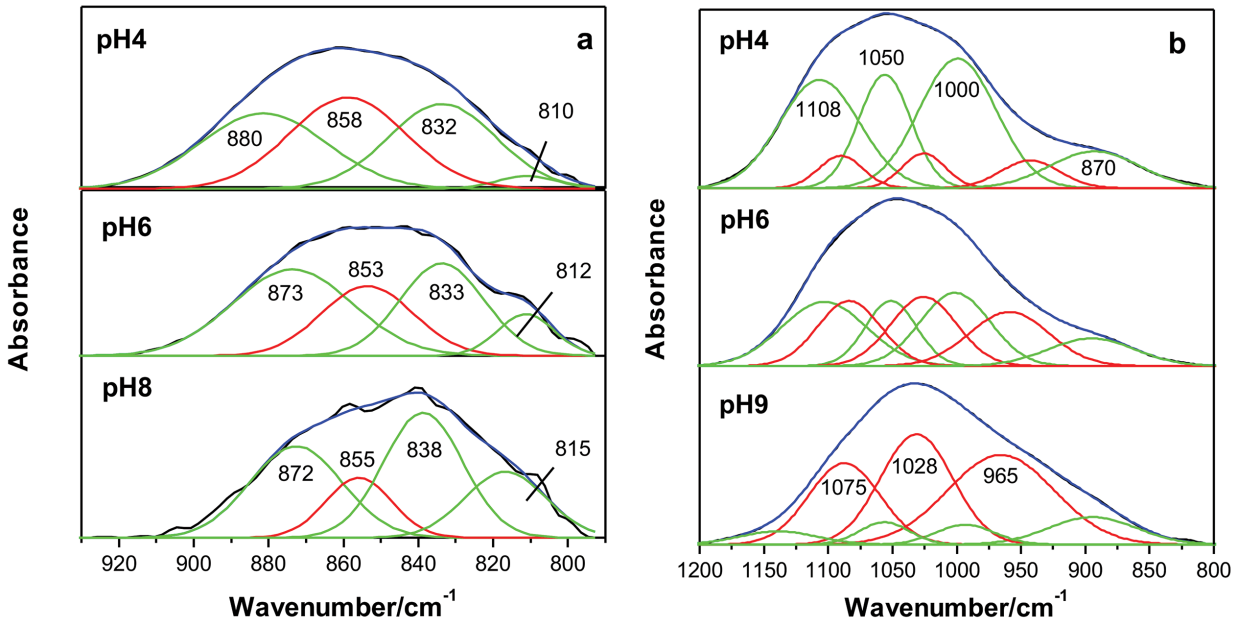

Figure 1. Infrared spectra for the individual adsorption of arsenate (**a**) and phosphate (**b**) on magnetite surface at acid, neutral, and alkaline conditions, as well as the spectral fitting with different adsorption species [arsenate: inner-sphere (green line) and outer-sphere (red line) species; phosphate: monoprotonated monodentate-mononuclear (green line) and non-protonated bidentate-binuclear complexes (red line)]. The total fit is represented by the blue line. (Color online.)

reported in the adsorption of phosphate on goethite (1089, 1044, and 945 cm^{-1}) (Kubicki et al. 2012) and hematite (1085, 1035, and 966 cm^{-1}) (Elzinga and Sparks 2007). The bands at 1075 and 1028 cm^{-1} were attributed to the stretching of the PO_2 bond, while the 965 cm^{-1} peak belonged to Fe-O-P bending.

$$2{\equiv}FeOH + HPO_4^{2-} \rightarrow (FeO)_2PO_2^- + H_2O + OH^- \quad (3)$$

The dominant complexes at acid pH were the protonated species. In previous studies, the characterization of their coordination environments and protonation degree were controversial (Arai and Sparks 2001; Elzinga and Sparks 2007; Luengo et al. 2006; Tejedortejedor and Anderson 1990), as the formations of $(XO_3)PO$ and $(XO_2)PO_2$ (X = Fe or H) were suggested. Protonated $(XO_3)PO$ species, including monoprotonated BB complexes [$(\equiv FeO)_2(OH)PO$, MBB] and di-protonated MM complexes ($\equiv FeO(OH)_2PO$, DMM), were reported for the adsorption on ferrihydrite (1124, 1035, and 998 cm^{-1}) (Carabante et al. 2010), goethite (1123, 1006, and 982 cm^{-1}) (Luengo et al. 2006; Tejedortejedor and Anderson 1990), and hematite (1120,

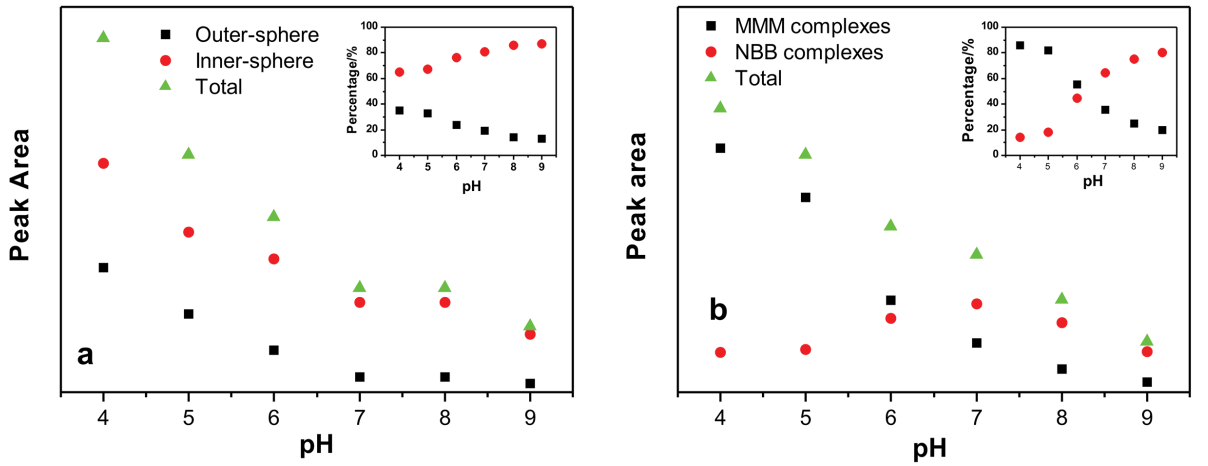

Figure 2. Integrated absorbance (IA) of the bands assigned to the adsorbed arsenate (**a**) and phosphate (**b**) plotted vs. pH, and the relative percentage of different adsorption species [arsenate: inner-sphere and outer-sphere species; phosphate: monoprotonated monodentate-mononuclear (MMM) and non-protonated bidentate-binuclear (NBB) complexes]. (Color online.)

1010, and 970 cm^{-1}) (Elzinga and Sparks 2007). The bands at high frequency (≥1120 cm^{-1}) were attributed to the P=O stretching of the $(XO_3)PO$ species (Arai and Sparks 2001; Elzinga and Sparks 2007). The adsorption geometry of protonated $(XO_2)PO_2$, i.e., monoprotonated MM [≡(FeO)(OH)PO_2], was identified on ferrihydrite (1100, 1028, and 920 cm^{-1}) (Arai and Sparks 2001) and hematite (1115, 1006, and 970 cm^{-1}) (Elzinga and Sparks 2007). For these complexes, bands at ~1100 and ~1115 cm^{-1} were assigned to the PO_2 group since its frequencies were between $\nu_{P=O}$ (1120 cm^{-1}) and $\nu_{P\text{-}OFe}$ (1000 cm^{-1}) (Tejedortejedor and Anderson 1990). In the present study, the phosphate complexes (1108, 1050, and 1000 cm^{-1}) that predominated at acid pH were monoprotonated MM complexes (MMM) (Eq. 4), as the band with the highest frequency (1108 cm^{-1}) was too low to be assigned to the P=O stretching. The bands at 1108 and 1050 cm^{-1} were attributed to the stretching of the PO_2 bond, while those at 1000 and 870 cm^{-1} belonged to the Fe-O-P and P-OH bending, respectively. The formation of the $FeOPO_3$ (C_{3v}) complexes were excluded, as they have a molecular symmetry higher than the lowest C_{2v} allowed.

$$\equiv FeOH + H_2PO_4^- \rightarrow \equiv FeO(PO_2)OH^- + H_2O \quad (4)$$

Competitive molecular adsorption

Substitution of phosphate by arsenate. At pH = 4, the MMM complexes are the dominant phosphate species followed by the NBB complexes (Fig. 2b). When the phosphate solution was substituted by an arsenate solution of equal molar concentration, the bands of phosphate (1200–870 cm^{-1}) immediately decreased in intensity, suggesting its desorption from the magnetite surface (upper panel of Fig. 3a). Simultaneously, the bands assigned to the adsorbed arsenate in the region of 900–800 cm^{-1} appeared and their intensity increased with the adsorption time. This became more obvious upon subtracting the equilibrium spectrum for the adsorbed arsenate recorded at 270 min from the signals recorded at 135 min, i.e., immediately before the introduction of arsenate. This subtraction highlighted only the bands for which intensity decreased (positive bands) or increased (negative bands) (lower panel of Fig. 3a). Based on the spectral integration, 32% of adsorbed phosphate was replaced by arsenate. The proportion of phosphate substituted by arsenate was close to the replacement found in previous studies using ferrihydrite and goethite (O'Reilly et al. 2001). For example, Carabante et al. reported that 35% of phosphate was desorbed from the ferrihydrite surface by arsenate using D_2O as solvent at pD = 4 (Carabante et al. 2010), while Liu et al. (2001) and Neupane et al. (2014) found that between 26–28% of the absorbed phosphate on goethite and ferrihydrite surfaces were replaced by arsenate. To determine the coordination environments, the positive bands in the range 1200–870 cm^{-1} were deconvoluted into three contributions at 1108, 1050, and 1000 cm^{-1}, which were assigned to MMM phosphate complexes. Moreover, the negative bands at 870, 827, and 801 cm^{-1} were attributed to arsenate BB complexes (Fig. 3a).

Similar competitive experiments were also conducted under neutral (pH = 7, Fig. 3b) and alkaline conditions (pH = 9, Fig. 3c), where partial substitution of phosphate by arsenate was also observed. At pH = 7.0, the amounts of phosphate adsorbed as MMM

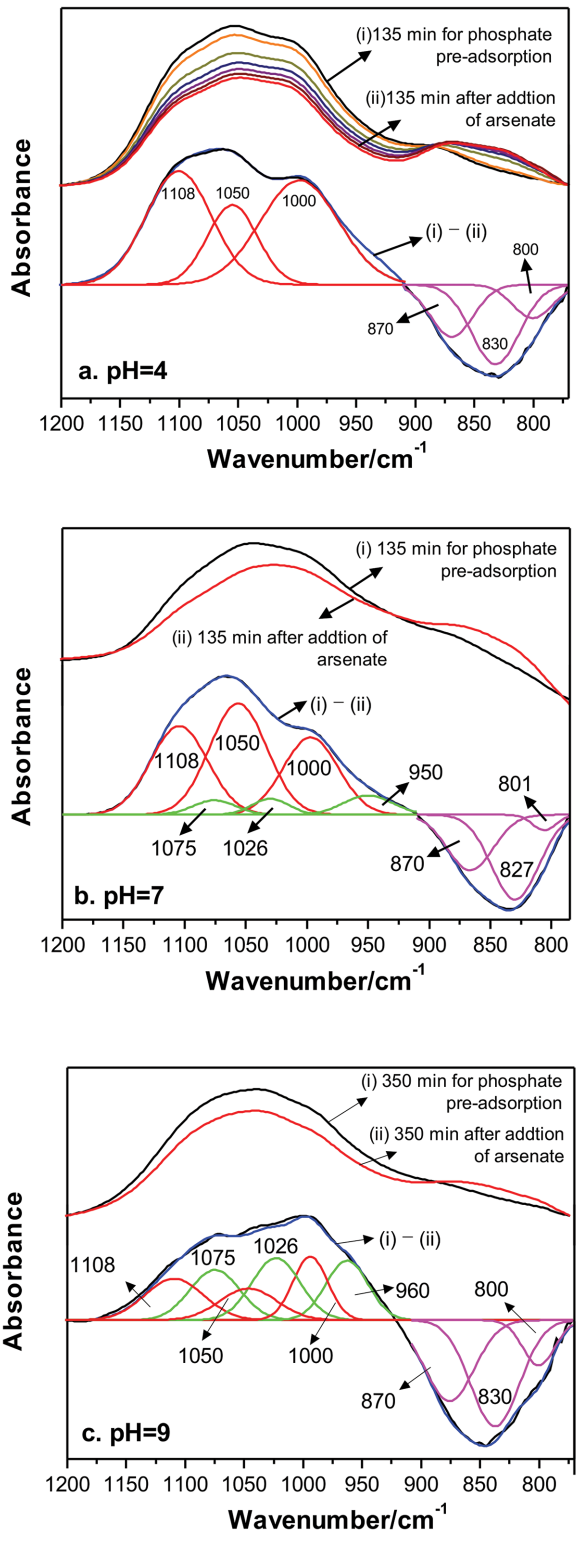

Figure 3. Infrared spectra of phosphate adsorbed onto magnetite at pH = 4 (**a**), pH = 7 (**b**), and pH = 9 (**c**). After 135 min (**a** and **b**) or 350 min (**c**), an arsenate solution at an equal (molar) concentration was added and the spectral change was monitored for another 135 min (**a** and **b**) or 350 min (**c**). (Color online.)

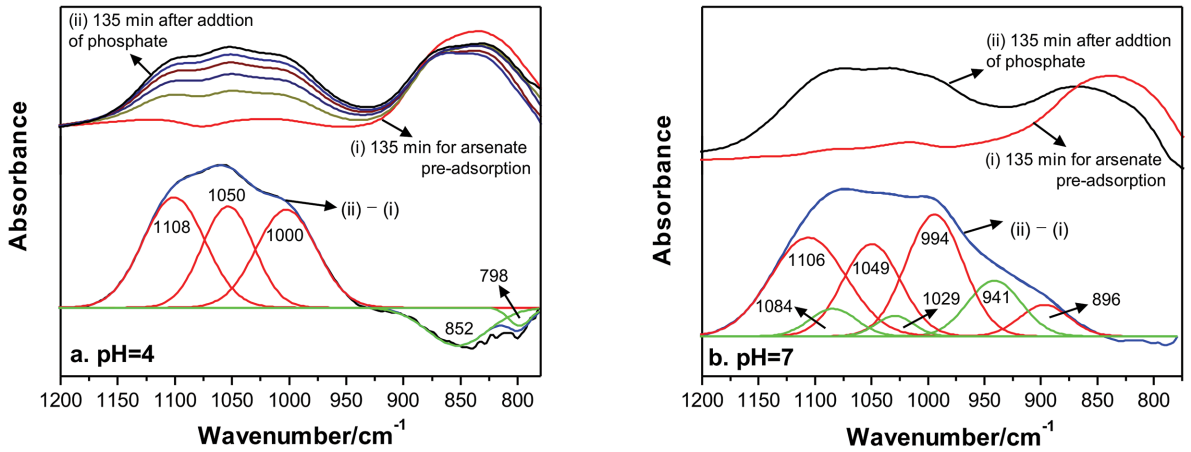

Figure 4. Infrared spectra of arsenate adsorbed onto magnetite at pH = 4 (**a**) and pH = 7 (**b**). After 135 min, a phosphate solution at an equal (molar) concentration was added and the spectral change was monitored for another 135 min (**a** and **b**) . (Color online.)

and NBB complexes were comparable (Fig. 2b). However, the integral spectrum of the NBB complexes (1075, 1026, and 960 cm^{-1}) was much lower than for the MMM complexes (1100, 1050, and 1000 cm^{-1}, Fig. 3b). The differences between the integrals of these bands indicate that the desorption of the MMM complexes was more significant than for the NBB, which was also found in the desorption of phosphate from ferrihydrite (Carabante et al. 2010).

To enhance the IR signal of the IS species at alkaline pH (Fig. 2), the concentrations of both phosphate and arsenate were increased from 100 to 500 μmol L^{-1} (Fig. 3c). The desorption of phosphate (~15%) was lower under alkaline conditions than at acid pH (~32%) (Fig. 3a), where the removal of both MMM and NBB complexes was comparable. Based on the integral area of the difference spectrum, the proportion of desorbed NBB complexes was below 15% of the total adsorbed phosphate. Moreover, the NBB complexes required 350 min to achieve desorption equilibrium, which was much slower than the removal of MMM at acid and neutral pH (135 min).

Substitution of arsenate by phosphate. At pH = 4, the adsorbed arsenate was mainly forming BB complexes, with a low proportion of OS species (Fig. 2a). After the introduction of phosphate solution of equal molar concentration, the bands in the region of 1200–900 cm^{-1} corresponding to phosphate appeared immediately and increased in intensity with time (Fig. 4a), illustrating adsorption on magnetite surfaces. However, the IR intensity of arsenate initially decreased slightly (~10%), but then stabilized, which suggests that the phosphate oxyanions can only substitute partially the pre-adsorbed arsenate. After subtracting the spectrum recorded just before the addition of phosphate and after its adsorption had reached equilibrium, at 135 and 270 min, respectively, the positive bands related to adsorbed phosphate were located at 1108, 1050, and 1000 cm^{-1}. As mentioned above, these bands were associated with the MMM phosphate complexes prevalent at acid pH. The negative bands that appeared at 852 and 798 cm^{-1} were attributed to the As-O asymmetrical stretching (ν_3) and the As-OH vibration of the arsenate OS species (Hu et al. 2015).

Similarly to the competitive adsorption at pH = 4, phosphate could not substitute the pre-adsorbed arsenate at neutral pH (Fig. 4b). The introduction of phosphate did not lead to a decrease in the IR intensity of arsenate. Although the individually absorbed phosphate species under neutral conditions were in equal proportions in both MMM and NBB geometries (Fig. 2b), only the former configuration was stable upon introduction of arsenate, as indicated by the phosphate bands at 1106, 1049, 994, and 896 cm^{-1}. Meanwhile, the difference spectrum did not show evidence of signals from the desorbed arsenate, which confirms that the arsenate BB complexes are the dominant adsorption configuration, with a higher binding affinity than both the MMM and NBB phosphate complexes.

At alkaline pH, the amount of arsenate that adsorbed onto magnetite was low, resulting in a poor signal-to-noise ratio for the spectra. Thus, competitive adsorption under alkaline conditions was not analyzed in this study.

Table 1. Adsorption sites, mean interatomic distances (*d*) and bond angles (∠) for the energetically preferred outer- (OS) and inner-sphere (IS) complexes of arsenate and phosphate at the Fe_3O_4(001) surface under both acid and alkaline conditions

Solute	pH	Adsorption site	*d*(*X*–O)[a] (Å)	*d*(*X*=O) (Å)	*d*(*X*O–H) (Å)	*d*(*X*O–Fe) (Å)	*d*(Fe–OH) (Å)	*d*(FeO–H) (Å)	∠(O–*X*–O) (°)	∠(O–*X* = O) (°)	∠(O=*X*=O) (°)	∠(*X*OH) (°)
$H_2AsO_4^-$	Acid	–	1.77	1.69	1.04	–	–	–	104.72	108.90	116.03	108.08
$HAsO_4$		Fe_B, Fe_B	1.76	1.72	1.05	2.06		1.02	–	107.31	111.54	112.97
$HAsO_4^{2-}$	Alkaline	–	1.76	1.72	1.01	–	1.92	0.99	–	109.81	109.06	109.42
$HAsO_4$		Fe_B, Fe_B	1.82	1.71	1.01	2.00	2.00	0.99	–	104.45	114.00	106.64
$H_2PO_4^-$	Acid	–	1.60	1.53	1.02	–	–	–	105.88	109.06	114.38	114.21
HPO_4		Fe_B	1.65	1.54	0.98	2.08	–	0.98	–	105.01	113.55	114.25
HPO_4^{2-}	Alkaline	–	1.60	1.54	1.03	–	1.95	0.97	–	106.99	111.87	120.38
PO_4		Fe_A, Fe_B	–	1.56	–	1.93	–	–	–	–	109.44	–

[a] *X* represents the central atom (P or As) of adsorbate.

TABLE 2. Adsorption sites, adsorption energies (E_{ads}) and charges (q) for the energetically preferred outer- (OS) and inner-sphere (IS) complexes of arsenate and phosphate at the Fe_3O_4(001) surface under both acid and alkaline conditions

Solute	pH	Adsorption site	E_{ads} (eV per molecule)	[a]$q(H_mXO_4)$ (e^-)	q(OH) (e^-)	q(H) (e^-)
$H_2AsO_4^-$	acid	–	–	–0.82	–	–
$HAsO_4$		Fe_B, Fe_B	–2.19	–1.42	–	0.67
$HAsO_4^{2-}$	alkaline	–	–	–1.52	–0.66	–
$HAsO_4$		Fe_B, Fe_B	–0.84	–1.38	–0.68	–
$H_2PO_4^-$	acid	–	–	–0.84	–	–
HPO_4		Fe_B	–1.89	–1.50	–	0.65
HPO_4^{2-}	alkaline	–	–	–1.54	–0.65	–
PO_4		Fe_A, Fe_B	–0.69	–2.13	–	–

[a] *X* represents the central atom (P or As) of adsorbate. *m* indicates the degree of protonation of the solute, which can take integer values from 0 to 3.

DFT calculations

Outer-sphere complexes. The outer-sphere (OS) complexes comprising the solute surrounded by water molecules are displayed in Online Material[1] Figure OM11. P-based anions are consistently smaller than their As-containing counterparts, as the intramolecular mean distance from the central atom to the oxygen ions differs by ~0.17 Å (Table 1). The degree of protonation of the solute does not noticeably affect the single and double bond distances (Table 1). As expected, the Bader charges of the solute ions are underestimated by ~17% with respect to their formal charges, which increases to ~23% with the pH value (Table 2). For the outer-sphere complexes under alkaline conditions, a charge of approximately –0.66 e^- was calculated for the OH groups (Table 2), which prefer to coordinate the protruding Fe_A ion at 1.92 and 1.95 Å for $HAsO_4^{2-}$ and HPO_4^{2-}, respectively (Online Material[1] Figure OM11).

Online Material[1] Figure OM11 displays the radial distribution functions for $H_2PO_4^-$, HPO_4^{2-}, $H_2AsO_4^-$, and $HAsO_4^{2-}$, where the radii are measured from the central atom of the P or As solute to the O of the water molecules. The main hydration shells for these oxyanions lie between 3.5 and 6.0 Å, which is in excellent agreement with the Molecular Dynamics (MD) simulations of Pathak and Bandyopadhyay (2016) for AsO_4^{3-} and supports the suitability of the size of our water simulation box (Pathak and Bandyopadhyay 2016). Under acid conditions, the di-protonated arsenate ($H_2AsO_4^-$) and phosphate ($H_2PO_4^-$) ions are the dominant species with C_{2v} symmetry and 15 fundamental vibrational modes. Alkaline pH values lead to the deprotonation of the outer-sphere complexes, thus increasing their symmetry to the C_{3v} molecular point group, with a reduction to 3 singly degenerate vibrations for the H atom. Generally, most of the fundamental vibrational modes for As-containing anions are red-shifted with respect to their phosphate counterparts, in excellent agreement with the ATR-FTIR experiments (Table 3). The only exceptions are the stretching ν(PO-H) and bending δ(POH) mode for HPO_4^{2-} and $H_2PO_4^-$, respectively, which appear at higher wavenumbers than for the iso-structural As-based molecules. However, taking into account that the bending δ(POH) is 1245 cm^{-1} for $H_2PO_4^-$ at acid pH (Table 3), which compares closely with the experimental value of 1240 cm^{-1} (Online Material[1] Figure OM8), we are confident of the predictive accuracy and consistency of our approximate vibrational modes. More details about the DFT results of outer-sphere complexes are described in Online Material[1] OM4.

Arsenate adsorption on the Fe_3O_4(001) surface. The dissociative adsorption process of the $H_2AsO_4^-$ solute onto the Fe_3O_4 (001) surface at acid pH can be represented as Equation 5:

$$Fe_{24}O_{32}(001)(s) + H_2AsO_4(aq) = Fe_{24}O_{31}(001)\cdot OH\cdot HAsO_4(s). \quad (5)$$

$HAsO_4^{2-}$ in the BB configuration is the most thermodynamically stable inner-sphere complex calculated for arsenate (Fig. 5a), with the largest adsorption energy of –2.19 eV per molecule (Table 2). The surface Fe_B ions coordinate the adsorbate O atoms at 2.06 Å, which reduces their electronic density and induces an elongation of the As=O bond distances by 0.03 Å with respect to the outer-sphere complexes. The O-As=O and particularly the O=As=O bond angles become narrower after adsorption, but the latter still remains wider than the former (Table 1). The dissociated proton binds a neighboring surface O atom at 1.02 Å, which is a slightly larger bond distance than in any of the other discussed solutes. The computed As-O bond

TABLE 3. Molecular point groups, adsorption sites and wavenumbers of the fundamental vibrational modes for the energetically preferred outer- (OS) and inner-sphere (IS) complexes of arsenate and phosphate at the Fe_3O_4(001) surface under both acid and alkaline conditions

Solute	pH	Sym	Adsorption site	ν(FeO–H) (cm^{-1})	[a]ν(*X*O–H) (cm^{-1})	δ(*X*OH) (cm^{-1})	ω(*X*OH) (cm^{-1})	ν(*X*=O) (cm^{-1})	ν(*X*–OH) (cm^{-1})	ν(*X*=OFe) (cm^{-1})	δ(FeOH) (cm^{-1})	ω(FeOH) (cm^{-1})
$H_2AsO_4^-$	Acid	C_{2v}	OS	–	3066	1372	1028	870	735	–	–	–
					2266	1268	756	817	666			
$HAsO_4^{2-}$		C_s	Fe_B, Fe_B	2875	2429	1291	1037	816	721	786	1042	1035
										751		
$HAsO_4^{2-}$	Alkaline	C_{3v}	OS	3365	3120	1190	776	830	728	–	1060	721
								790				
								756				
$HAsO_4^{2-}$		C_s	Fe_B, Fe_B	3458	3007	1278	830	792	624	810	928	797
										782		
$H_2PO_4^-$	Acid	C_{2v}	OS	–	2826	1269	938	1096	904	–	–	–
					2742	1221	920	1012	839			
HPO_4^{2-}		C_s	Fe_B	3350	3625	1018	–	1088	766	942	1170	706
								1045				
HPO_4^{2-}	Alkaline	C_{3v}	OS	3739	2626	1271	947	1045	867	–	718	616
								1003				
								926				
PO_4^{3-}		C_s	Fe_A, Fe_B	–	–	–	–	1112	–	909	–	–
								949		884		

Notes: The presented vibrational frequencies are stretching (ν), bending (δ), and wagging (ω).
[a] *X* represents the central atom (P or As) of adsorbate.

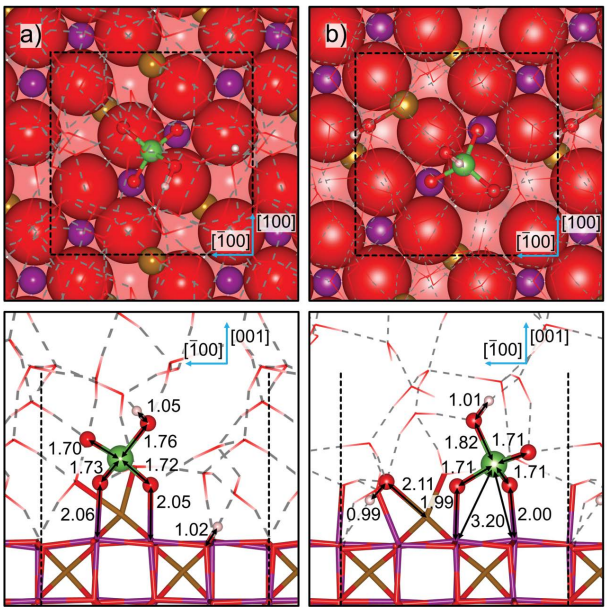

Figure 5. Top and side views of the aqueous inner-sphere species $HAsO_4^{2-}$ under (**a**) acid and (**b**) alkaline conditions. Tetrahedral Fe_A atoms are in orange, octahedral Fe_B atoms are in violet, O atoms are in red, As atoms are in green, and H atoms are in pink. Surface atoms are represented as (top panels) balls and (bottom panels) sticks, water solvent molecules are represented as wireframe and the solute molecules are represented as balls-and-sticks. Light and dark dashed lines mark hydrogen bonds and the limits of the computational cell, respectively. The double arrows indicate interatomic distances in angstroms. (Color online.)

length and As-Fe distance of the BB arsenate complex are ca. 1.71 and 3.20 Å, respectively, which is consistent with the values (1.69 and 3.42 Å) obtained from EXAFS analysis (Jonsson and Sherman 2008).

The acid proton has a typical charge of 0.67 e^-, while the inner-sphere complexes gain 0.60 e^- compared to the di-protonated molecule in solution. Consistent with the presence of two types of H atoms, i.e., in the inner-sphere complexes and directly attached to the surface, six singly degenerate vibrational modes associated with these atoms are found (Table 3). The stretching ν(AsO-H) and bending δ(AsOH) in the adsorbed molecule are red-shifted with regard to the outer-sphere complexes, in line with their different chemical environments. The stretching modes involving the central As atom have the typical pattern of BB complexes. For instance, the largest wavenumber of 816 cm^{-1} is assigned to the As=O bond, whereas the intermediate vibrations between 751 and 786 cm^{-1} are calculated for the symmetric and asymmetric ν(As-OFe). In agreement with its largest distance, the softer mode is computed for the single bond between the central atom and the protonated oxygen.

Unlike the outer-sphere $H_2AsO_4^-$ complexes, which adsorb dissociatively in acid environment, the $HAsO_4^{2-}$ anion does not change its stoichiometry after binding to the $Fe_3O_4(001)$ surface at alkaline pH (Eq. 6):

$$Fe_{24}O_{32}(001)\cdot OH(s) + HAsO_4(aq) = Fe_{24}O_{32}(001)\cdot OH\cdot HAsO_4(s). \quad (6)$$

The mono-protonated adsorbed As-containing molecule interacts with two Fe_B surface ions, forming a bidentate (BB) configuration that resembles the inner-sphere complexes of arsenate at acid pH (Fig. 5b).

However, the presence of an adsorbed OH^- group rather than H^+ causes noticeable energetic and structural changes in the adsorbate. The adsorption energy increases by 1.35 eV per $HAsO_4^{2-}$ molecule when the pH changes from acid to alkaline, becoming comparable to the experimental value reported by Sabur and coworkers for arsenate at neutral pH conditions (Sabur et al. 2015). The Fe_B-O bonds between the molecule and surface are 0.07 Å shorter at high than at low pH. The bond distance from the central As atom to the hydroxy group is stretched from 1.76 to 1.86 Å following the increase in pH. After adsorption, the OH group moves 0.08 Å away from the surface and leans toward a nearby surface O atom to form a hydrogen bond. Table 1 shows that the relative order ∠(O-As=O) < ∠(O=As=O) is restored for the bond angles upon the formation of the inner-sphere complexes. Despite the same stoichiometry, the Bader charge analysis reveals that the adsorbate loses 0.14 e^- after adsorption, but the charge of the OH^- remains almost unaffected at –0.68 e^-.

Owing to the similar adsorption configuration for $HAsO_4^{2-}$ at both acid and alkaline pH, the number and type of fundamental vibrational modes under these two conditions are the same. However, all vibrations shift for $HAsO_4^{2-}$ as a result of the change in pH (Table 3). For example, the wavenumber for ν(As-OH) increases greatly to 3007 cm^{-1}, whereas ω(AsOH) is red-shifted to 830 cm^{-1}. The increase in pH has a strong impact on the stretching mode of the elongated As-OH bond of the surface-immobilized $HAsO_4^{2-}$ species. Moreover, the formation of the inner-sphere arsenate complexes and FeOH···H hydrogen bond have a major effect on the ν(FeO-H) and ω(FeOH) modes. Our DFT predicted vibrational frequencies for the hardest modes ν(As=O) and ν(As=OFe) of the inner-sphere $HAsO_4^{2-}$ complex under both acid and alkaline conditions are under-estimated by ~60 cm^{-1} with respect to the experimental values. However, the deviation between the ATR-FTIR spectra and the simulated frequency is 90 and 190 cm^{-1} under acid and alkaline conditions, respectively, for the softer mode ν(As-OH).

Phosphate adsorption on the Fe_3O_4(001) surface. Among the various possible binding geometries of phosphate onto magnetite, the mono-protonated monodentate mononuclear (MMM) mode is the most stable adsorption configuration at acid pH, wherein the HPO_4^{2-} anion binds the Fe_B surface cation and releases 1.89 eV per molecule (Table 2; Fig. 6a). The dissociative adsorption of $H_2PO_4^-$ on the $Fe_3O_4(001)$ surface at acid conditions can be represented by Eq. (7):

$$Fe_{24}O_{32}(001)(s) + H_2PO_4(aq) = Fe_{24}O_{31}(001)OH\cdot HPO_4(s) \quad (7)$$

As shown in Figure 6a, the dissociated proton prefers to interact at 0.98 Å with a nearby surface oxygen atom to form acid $Fe_{24}O_{31}(001)\cdot OH$ groups rather than H_3O^+ cations in solution. The strong chemisorption is characterized by the adsorbate-surface PO-Fe_B interatomic bond distance of 2.08 Å, which is only 0.02 Å larger than the O-Fe_B distance in the bulk of Fe_3O_4 (Table 1). The average P=O distances for the outer- and

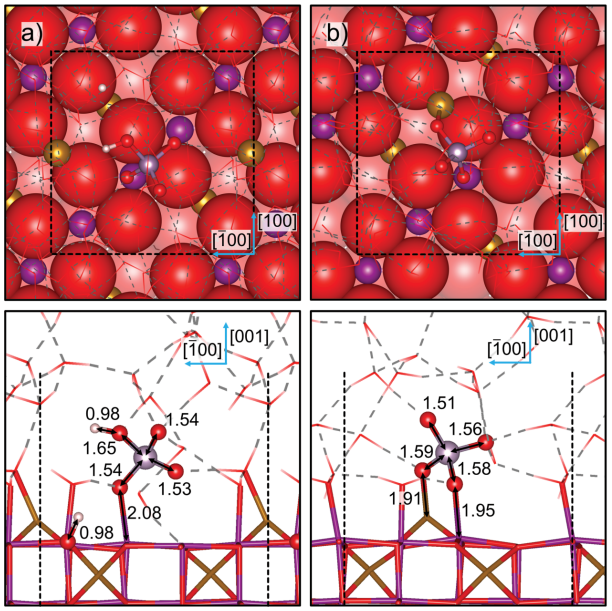

Figure 6. Top and side views of the aqueous inner-sphere species (**a**) HPO_4^{2-} and (**b**) PO_4^{3-} under acid and alkaline conditions, respectively. Tetrahedral Fe_A atoms are in orange, octahedral Fe_B atoms are in violet, O atoms are in red, P atoms are in blue, and H atoms are in pink. Surface atoms are represented as (top panels) balls and (bottom panels) sticks, water solvent molecules are represented as wireframe and the solute molecules are represented as balls-and-sticks. Light and dark dashed lines mark hydrogen bonds and the limits of the computational cell, respectively. The double arrows indicate interatomic distances in angstroms. (Color online.)

inner-sphere P-containing complexes are very close at acid pH. Compared to $H_2PO_4^-$ in solution, the P-O bond stretches, whereas the PO-H bond distance decreases by ~0.05 Å for the adsorbed HPO_4^{2-}. The O-P=O bond angle experiences the largest change, from 109.06° to 105.01°, given that the adsorbate loses half of its single-bonded O atoms during the dissociative adsorption of $H_2PO_4^-$. The charge of the dissociated H is 0.65 e^-, while the adsorbed anion becomes 0.66 e^- more negative than its parent ion in solution (Table 2).

Dissociative adsorption of $H_2PO_4^-$ in the MMM configuration causes its molecular point group to reduce to C_s and to a total number of 12 fundamental vibrational modes. After binding to the surface, the POH wagging is not detected above 600 cm^{-1}, while the PO-H stretching is shifted to 3625 cm^{-1} and the POH bending is red-shifted by approximately 200 cm^{-1} (Table 3). In line with the new symmetry, the two largest stretching modes are assigned to $P=O_2$, whereas 942 cm^{-1} corresponds to P-OFe, and the lowest wavenumber is calculated for the protonated O atom. For the dissociated proton, the FeO-H stretching as well as the FeOH bending and wagging were obtained at the usual position for OH groups. The calculated vibrational frequencies were also underestimated for the inner-sphere phosphate complexes under acid conditions, with the largest discrepancy observed for the modes with the smallest wavenumber. For example, the simulated values for the hardest ν(P=O) modes were just 5 and 20 cm^{-1} below the experimental frequencies; while the difference for the softer (softest) ν(P=OFe) [ν(P-OH)] mode was 60 (104) cm^{-1}.

Under alkaline conditions, HPO_4^{2-} prefers to adsorb dissociatively onto the $Fe_3O_4(001)$ surface, forming the non-protonated bidentate binuclear (NBB) inner-sphere complex and liquid water as follows:

$$Fe_{24}O_{32}(001)\cdot OH(s) + HPO_4(aq) = Fe_{24}O_{32}(001)\cdot PO_4(s) + H_2O(l). \quad (8)$$

This process releases 0.69 eV per molecule, which is the weakest adsorption energy reported in this study (Table 2). Two O atoms from the anion coordinate the surface Fe_A and Fe_B ions at 1.91 and 1.95 Å, respectively (Table 1; Fig. 6b). A small stretch in the P=O bond from the average value of 1.56 Å is also observed in those atoms directly interacting with the surface, whereas the bond angles remain perfectly tetrahedral at 109.44 °. The Bader charge for the inner-sphere PO_4^{3-} complex is –2.13 e^-, which is the largest reported in this paper. The charge of the fully deprotonated phosphate ion explains its small adsorption energy, caused by the strong Coulombic repulsion at the negatively charged $Fe_3O_4(001)$ surface. The PZC of magnetite at 6.8 suggests that at alkaline pH, the Fe_3O_4 surfaces become negative due to adsorbed OH^- groups.

Despite its C_s point group, the adsorbed NBB PO_4^{3-} species has the simplest set of vibrational frequencies with only 4 measurable fundamental modes (Table 3). The largest frequencies are for the asymmetric and symmetric P=O modes, at 1111.64 and 948.85 cm^{-1}, respectively. The longest and weakest P-OFe bonds are characterized by the smallest frequencies, which were calculated at 909 and 884 cm^{-1} for the asymmetric and symmetric modes, respectively.

Although phosphate OS complexes are smaller than their arsenate counterparts (Table 1), the three solvation shells found are formed roughly at the same distance from the central atom for the two different oxyanions, which essentially remain tetrahedral. However, when the phosphate and arsenate molecules approach the $Fe_3O_4(001)$ surface, they form IS complexes of different geometries and numbers of interactions with the exposed Fe ions. The adsorption energies show that under both acid and alkaline conditions arsenate prefers to form MBB complexes with two neighboring Fe_B ions from the $Fe_3O_4(001)$ surface. However, phosphate forms an NBB complex with the exposed Fe_A and Fe_B ions at alkaline pH, while HPO_3^{2-} coordinates a single Fe_B ion as an MMM species under acid conditions (Figs. 6 and 7). On thermodynamic grounds, arsenate species bind more strongly to the $Fe_3O_4(001)$ surface than the phosphate complexes under acid and alkaline conditions (Table 2), which explains the stronger adsorption affinity of arsenate over phosphate. The oxyanions release the largest adsorption energies under acid conditions, and the calculated Bader charges explain the trends found for the adsorption energies. Adsorption reduces the molecular point group of the oxyanions, which impacts the frequency of the four stretching modes involving the central atom and the oxygen atoms (Table 3). The shift of the vibrational modes for the adsorbed oxyanions with respect to the OS complexes offers an unambiguous route to characterize the geometry and coordination number of the IS species.

Effect of pH on individual and comparative adsorption. During individual molecular adsorption of equal amounts of arsenate and phosphate, their adsorption edges have very similar curve profiles, in agreement with previous works (Arai and Sparks 2001; Jia et al. 2007; Luengo et al. 2006). In this study, the arsenate and phosphate adsorption increased gradually on magnetite as the pH decreased (Online Material[1] Figs. OM3 and OM6), ascribed to the positive charge of the mineral surface. Such variations have also been observed in the individual adsorption of arsenate and phosphate onto goethite, which is the most studied mineral adsorbent (Hingston et al. 1971; Liu et al. 2001; Manning and Goldberg 1996). As reported by Liu et al. (2001) the surface coverage of phosphate and arsenate on goethite was 112 and 109 mol kg^{-1} at pH = 8, respectively, which increased to 193 and 197 mol kg^{-1} at pH = 3. Although the individual arsenate and phosphate adsorption showed similar dependence on the pH, the binding efficiency was greatly affected by pH during competitive adsorption. In this study, when pre-adsorbed on magnetite, 32% of phosphate was desorbed in the presence of arsenate at pH = 4 (Fig. 5), while only 15% was desorbed at pH = 9 (Fig. 7). The phosphate adsorption strength increased with pH, which was also observed during adsorption onto goethite and ferrihydrite. Liu et al. (2001) found that, in the presence of arsenate, the efficiency of phosphate adsorption on goethite increased from 50% (pH = 3) to 70% (pH = 8) and was not significantly influenced at alkaline pH, i.e., 69% (pH = 7), 70% (pH = 8), and 72% (pH = 9). To evaluate the ability of phosphate (or arsenate) to depress the adsorption of arsenate (or phosphate) during competitive adsorption, the competition efficiency (%) of phosphate η_P was calculated as $\eta_P = 100 \times (1 - N_{arsenate}/N^{o}_{arsenate})$, where $N_{arsenate}$ was the amount of arsenate adsorbed in the presence of phosphate and $N^{o}_{arsenate}$ was the amount of arsenate individually adsorbed (Liu et al. 2001). The obtained results show that, independently of pH, the competition efficiency of arsenate over phosphate ranged from 70 to 74%. In contrast, phosphate was more stable under alkaline than acid conditions.

The pH effect on the competitive adsorption efficiency between phosphate and arsenate has been observed in previous studies. For example, in soils, the inhibitory effect of phosphate toward arsenate adsorption is stronger than the other way round when the pH is higher than 6 (Melamed et al. 1995; Peryea 1991). Gao and Mucci reported that the phosphate introduction obviously restrained the arsenate adsorption on goethite at alkaline pH. The arsenate addition, even in excess, led to only slight decrease in the amount of phosphate adsorbed (Gao and Mucci 2001). These findings are different from ours, where the individual arsenate and phosphate adsorptions were found to be comparable at alkaline pH. However, the affinity toward goethite is stronger for arsenate than for phosphate at acid pH (Carabante et al. 2009; Violante and Pigna 2002; Zhao and Stanforth 2001), which becomes comparable under neutral conditions (Manning and Goldberg 1996). Therefore, pH plays a vital role in the competitive adsorption between arsenate and phosphate.

Effect of adsorption sequence on individual and comparative adsorption. The simultaneous or successive addition of oxyanions is important in the context of competitive adsorption (Carabante et al. 2010; Liu et al. 2001). In nature, environmental substances are more commonly adsorbed onto minerals sequentially than simultaneously. When pre-adsorbed arsenate was replaced by phosphate on goethite, the competition efficiency of arsenate and phosphate remained constant at 70–74% and 20%, respectively, independent of pH (Liu et al. 2001). However, substitution of pre-adsorbed phosphate by arsenate led to an increase of the competition efficiency of phosphate from 50% (acid pH) to 65% (alkaline pH), while arsenate decreased from 30% (acid pH) to 10% (neutral pH). For the simultaneous addition of the adsorbates, the efficiency of arsenate and phosphate was 50% and 40%, respectively. Although the competitive adsorption experiment was carried out using different adsorption sequences, arsenate was always adsorbed more strongly than phosphate, indicating that arsenate has the highest affinity toward the goethite surfaces. This was also found during the competitive arsenate and phosphate adsorption onto magnetite and ferrihydrite (Carabante et al. 2010). For example, as reported in this study, the amount of phosphate adsorbed decreased by 32% after the introduction of arsenate at equal concentration under acid conditions. Conversely, the subsequent addition of phosphate only resulted in about 10% arsenate desorption. This is consistent with the results from the DFT calculations, where it was found that arsenate has stronger adsorption affinity to magnetite than phosphate.

Effect of mineral species on individual and comparative adsorption. Diverse competitive adsorption trends appear for phosphate and arsenate during interaction with different mineral phases in soils. In general, the competitive ability toward iron (hydr)oxides is stronger for arsenate than for phosphate. As mentioned above, during the adsorption on ferrihydrite and goethite, the restraining effect of arsenate on phosphate is obviously the strongest. A similar phenomenon is also seen in this study, where arsenate has higher affinity for and stability on magnetite than phosphate. However, the opposite was found when aluminum (hydr)oxides were the mineral phases. Manning and Goldberg (1996) investigated competitive adsorption of arsenate and phosphate on goethite and gibbsite. On both mineral phases, phosphate induced the desorption of ca. 15 mmol kg^{-1} of arsenate. However, the arsenate addition only decreased the phosphate adsorption by 8 mmol kg^{-1} on gibbsite, which indicates a preference for phosphate rather than arsenate. The arsenate and phosphate also display similar competitive adsorption on calcite and aluminum (hydr)oxides. The arsenate adsorption is significantly inhibited by phosphate, while the phosphate adsorption is barely affected by arsenate (So et al. 2012).

In addition to the chemical composition of the mineral phases, the competitive adsorption properties of arsenate and phosphate are also affected by the crystallinity of the material. Xu et al. (2008) studied the effect of arsenate addition on the phosphate desorption kinetics from crystalline and amorphous hydrargillite. Phosphate was easily replaced by arsenate, which had the largest affinity for amorphous rather than for crystalline hydrargillite, because of difference in the density of surface-active sites.

Competitive adsorption mechanism. Despite the similar individual adsorption behavior, the mechanism for the competitive adsorption between arsenate and phosphate onto the iron (hydr)oxide surfaces is still a topic of debate. Phosphate with its smaller thermochemical radius is expected to have the strongest affinity for these mineral phases, yet arsenate displays the strongest preference, especially at acid pH.

During arsenate and phosphate adsorption onto iron (hydr)oxides, these oxyanions adopt diverse geometries with different binding strengths. For example, phosphate adsorbed on ferrihydrite displays two adsorption geometries, i.e., protonated BB and non-protonated BB, as observed by in situ ATR-FTIR (Carabante et al. 2010). Arsenate is mainly adsorbed in the BM and BB geometries, as determined by in situ ATR-FTIR and XAFS (Carabante et al. 2010; Neupane et al. 2014). However, these adsorption complexes display different affinities toward mineral surfaces. For example, phosphate induces the desorption of the BM arsenate complexes, while the BB arsenate complexes are less affected (Neupane et al. 2014), which indicates that the stability is higher for the BB than for the BM arsenate species.

In this study, in situ ATR-FTIR and DFT calculations have revealed that phosphate was individually adsorbed onto magnetite in the NBB and MMM geometries, while arsenate mainly formed BB complexes with few OS species. However, under competitive adsorption conditions, the BB arsenate complexes obviously substituted both the MMM and to a lesser extent the NBB phosphate complexes. These findings illustrate that NBB phosphate complexes are more stable than MMM complexes, and also that their binding strength is weaker than for the BB arsenate complexes. The competitive adsorption of phosphate and arsenate can be explained by variations in adsorption geometries with pH. Under acid conditions, the dominant MMM phosphate species had the smallest adsorption energies (E_{ads} = –0.69 eV, Table 2) and were easily replaced by arsenate (E_{ads} = –0.84 eV). As pH increased, NBB became the main phosphate species, displaying enhanced stability (E_{ads} = –1.89 eV), which resulted in decreasing desorption by arsenate. Throughout the studied pH range, the adsorbed arsenate remained in the BB geometry with higher stability than phosphate. Thus, the competitive efficiency for phosphate increased with pH, while for arsenate it remained almost stable. These results for magnetite are in excellent agreement with the findings on goethite (Liu et al. 2001).

Besides the adsorption geometry, the Coulombic interaction between the positively charged magnetite surfaces and negatively charged adsorbates is another important factor controlling the competitive adsorption between arsenate and phosphate. Given the magnetite PZC at 6.8, the electrostatic attraction with phosphate and arsenate oxyanions increases as pH decreases. This improves the adsorption onto the magnetite surface and thus, decreases the proportion of hydroxyl groups covering adsorption sites. The adsorption geometry of phosphate species changes from NBB to MMM complexes, which contain fewer protons. A similar variation in adsorption complexation from binuclear to mononuclear is also observed during the adsorption of arsenate onto ferrihydrite (Neupane et al. 2014). To form BB complexes with higher stability than MM configurations, the oxyanions should be bound to two adjacent protonated oxygen sites. However, only mononuclear complexes are formed if the protonated oxygen site is far away from the adsorbate. Based on the shorter intramolecular O···O distance in phosphate compared to arsenate (2.45 and 2.6–2.8 Å, respectively), the latter is more likely to form BB complexes than the former (So et al. 2012). Lumsdon et al. (1984) found that the interaction with hydroxyl sites was stronger for arsenate than for phosphate, because of the different molecular sizes of the adsorbates. Thus, arsenate bidentate binuclear complexes dominate in areas of high surface coverage, whereas monodentate species are only found in areas of low surface coverage (Fendorf et al. 1997). In contrast, the large surface coverage of phosphate species prefers the formation of monodentate complexes (Liu et al. 2001), which was also found under the acidic condition in this study.

Compared to other iron oxides, the formation of abundant monodentate mononuclear phosphate complexes on magnetite alongside a low proportion of arsenate OS species is unique for this combination of substrate and adsorbates. The PZC value for magnetite (~6.8) is lower than for goethite (~9.1), ferrihydrite (~7.6–8.1), or hematite (~11), which leads to Fe_3O_4 displaying a lower degree of protonation than other iron oxides at the same pH. Protonated surface sites facilitate IS surface complexation because water is more easily displaced than hydroxyl groups (Johnston and Chrysochoou 2012). Thus, the decrease of protonation on the magnetite surface results in the formation of more MM complexes of phosphate with fewer hydroxyl groups, as well as OS species of arsenate. Similar variations have appeared in sulfate adsorption, where IS complexes are exclusively found on hematite with the highest PZC (Hug 1997), and both OS and IS complexes are formed on ferrihydrite (Johnston and Chrysochoou 2014).

Implications

This study provides a molecular-level insight into the competitive adsorption between arsenate and phosphate on magnetite surfaces. Magnetite has a widespread occurrence in surface environment and is found coating the zero-valent iron nanoparticles increasingly used for environmental engineering, especially for As removal. Thus, our new results would be beneficial for assessing the environmental fate of arsenate and phosphate, as well as for other ions that may compete for or otherwise react with the magnetite surface sites.

Owing to the low-surface site density of magnetite, its adsorption toward oxyanions has seldom been surveyed by in situ techniques. In this study, with the aid of 2D-COS analysis, we have resolved better the peaks of in situ ATR-FTIR spectra, which greatly facilitates the identification of adsorption species and geometries of both oxyanions. For phosphate, mono-protonated monodentate mononuclear (MMM) complexes dominated at acid pH, while non-protonated bidentate binuclear (NBB) complexes were dominant at alkaline conditions. Arsenate mainly formed bidentate binuclear (BB) complexes with some outer-sphere species, both of which were more prevalent at acid than at alkaline pH. This is somewhat different from the cases on other iron oxides, e.g., ferrihydrite and goethite, ascribed to the lower surface site density of magnetite. The competitive adsorption of these adsorption species was further investigated by ATR-FTIR for different substitution sequences, providing spectroscopic evidence for their adsorption affinity toward magnetite surface. The adsorption strength was also thermodynamically confirmed for the first time through DFT calculations. Therefore, this study offers an important step forward in understanding the adsorption of oxyanions in complex systems, which is more environmentally realistic.

The adsorption affinity of the geometries as observed increased in the following order: MMM phosphate complex < NBB

phosphate complex < BB arsenate complex. The high stability of adsorbed arsenate suggests the vital role of magnetite in the transfer and transformation of arsenic in the surface environment. Meanwhile, magnetite could be used as an arsenic scavenger for in situ remediation of phosphate-rich groundwater and soil.

Funding

This work was financially supported by the National Key Research and Development Program of China (Grant No. 2017YFC0602306), the National Natural Science Foundation of China (Grant Nos. 41773113 and 41825003), Natural Science Foundation for Distinguished Young Scientists of Guangdong Province (Grant No. 2020B1515020015), Science and Technology Program of Guangzhou, China (Grant No. 201804020037), and the Youth Innovation Promotion Association CAS (Grant No. Y201863), Science and Technology Planning of Guangdong Province, China (Grant No. 2020B1212060055). This work is Contribution No. IS-2967 from GIGCAS. D.S.-C. and N.H.d.L. acknowledge the Engineering and Physical Sciences Research Council (EPSRC, Grant No. EP/K009567) for funding. Via our membership of the U.K.'s HEC Materials Chemistry Consortium, which is funded by EPSRC (Grant No. EP/L000202 and EP/R029431), this work used the ARCHER UK National Supercomputing Service (http://www.archer.ac.uk). This work also used the computational facilities of the Advanced Research Computing @ Cardiff (ARCCA) Division, Cardiff University. This research was undertaken using the Supercomputing Facilities at Cardiff University operated by ARCCA on behalf of the Cardiff Supercomputing Facility, HPC Wales and Supercomputing Wales (SCW) projects. We acknowledge the support of the latter, which is part-funded by the European Regional Development Fund (ERDF) via Welsh Government. All data created during this research is openly available from the Cardiff University's Research Portal at http://doi.org/10.17035/d.2019.0081529534.

References cited

Anisimov, V.I., Korotin, M.A., Zaanen, J., and Andersen, O.K. (1992) Spin bags, polarons, and impurity potentials in $La_{2-x}Sr_xCuO_4$ from first principles. Physical Review Letters, 68(3), 345–348.

Antelo, J., Arce, F., and Fiol, S. (2015) Arsenate and phosphate adsorption on ferrihydrite nanoparticles. Synergetic interaction with calcium ions. Chemical Geology, 410, 53–62.

Arai, Y., and Sparks, D.L. (2001) ATR-FTIR spectroscopic investigation on phosphate adsorption mechanisms at the ferrihydrite-water interface. Journal of Colloid and Interface Science, 241(2), 317–326.

Blochl, P.E. (1994) Projector augmented-wave method. Physical Review B, 50(24), 17953–17979.

Brechbuhl, Y., Christl, I., Elzinga, E.J., and Kretzschmar, R. (2012) Competitive sorption of carbonate and arsenic to hematite: Combined ATR-FTIR and batch experiments. Journal of Colloid and Interface Science, 377, 313–321.

Carabante, I., Grahn, M., Holmgren, A., Kumpiene, J., and Hedlund, J. (2009) Adsorption of As (V) on iron oxide nanoparticle films studied by in situ ATR-FTIR spectroscopy. Colloids and Surfaces a-Physicochemical and Engineering Aspects, 346(1-3), 106–113.

Carabante, I., Grahn, M., Holmgren, A., and Hedlund, J. (2010) In situ ATR-FTIR studies on the competitive adsorption of arsenate and phosphate on ferrihydrite. Journal of Colloid and Interface Science, 351(2), 523–531.

Catalano, J.G., Park, C., Fenter, P., and Zhang, Z. (2008) Simultaneous inner- and outer-sphere arsenate adsorption on corundum and hematite. Geochimica et Cosmochimica Acta, 72(8), 1986–2004.

Chakraborti, D., Rahman, M.M., Paul, K., Chowdhury, U.K., Sengupta, M.K., Lodh, D., Chanda, C.R., Saha, K.C., and Mukherjee, S.C. (2002) Arsenic calamity in the Indian subcontinent—What lessons have been learned? Talanta, 58(1), 3–22.

Choppala, G., Bolan, N., Kunhikrishnan, A., and Bush, R. (2016) Differential effect of biochar upon reduction-induced mobility and bioavailability of arsenate and chromate. Chemosphere, 144, 374–381.

Correll, D.L. (1998) The role of phosphorus in the eutrophication of receiving waters: A review. Journal of Environmental Quality, 27(2), 261–266.

da Silva, J.J.R. Frausto and Williams, R.J.P. (2001) The Biological Chemistry of the Elements: The inorganic chemistry of life. 2nd ed. 62–63 p. Oxford University Press.

Dudarev, S.L., Botton, G.A., Savrasov, S.Y., Humphreys, C.J., and Sutton, A.P. (1998) Electron-energy-loss spectra and the structural stability of nickel oxide: An LSDA+U study. Physical Review B, 57(3), 1505–1509.

Dupuis, C., and Beaudoin, G. (2011) Discriminant diagrams for iron oxide trace element fingerprinting of mineral deposit types. Mineralium Deposita, 46(4), 319–335.

Elzinga, E.J., and Sparks, D.L. (2007) Phosphate adsorption onto hematite: An in situ ATR-FTIR investigation of the effects of pH and loading level on the mode of phosphate surface complexation. Journal of Colloid and Interface Science, 308(1), 53–70.

Fendorf, S., Eick, M.J., Grossl, P., and Sparks, D.L. (1997) Arsenate and chromate retention mechanisms on goethite.1. Surface structure. Environmental Science and Technology, 31(2), 315–320.

Filip, J., Karlicky, F., Marusak, Z., Lazar, P., Cernik, M., Otyepka, M., and Zboril, R. (2014) Anaerobic reaction of nanoscale zerovalent iron with water: Mechanism and kinetics. Journal of Physical Chemistry C, 118(25), 13817–13825.

Gao, Y., and Mucci, A. (2001) Acid base reactions, phosphate and arsenate complexation, and their competitive adsorption at the surface of goethite in 0.7 M NaCl solution. Geochimica et Cosmochimica Acta, 65(14), 2361–2378.

Gao, X.D., Root, R.A., Farrell, J., Ela, W., and Chorover, J. (2013) Effect of silicic acid on arsenate and arsenite retention mechanisms on 6-L ferrihydrite: A spectroscopic and batch adsorption approach. Applied Geochemistry, 38, 110–120.

Gorski, C.A., Nurmi, J.T., Tratnyek, P.G., Hofstetter, T.B., and Scherer, M.M. (2010) Redox behavior of magnetite: Implications for contaminant reduction. Environmental Science and Technology, 44(1), 55–60.

Grimme, S. (2006) Semiempirical GGA-type density functional constructed with a long-range dispersion correction. Journal of Computational Chemistry, 27(15), 1787–1799.

Grossl, P.R., Eick, M., Sparks, D.L., Goldberg, S., and Ainsworth, C.C. (1997) Arsenate and chromate retention mechanisms on goethite.2. Kinetic evaluation using a pressure-jump relaxation technique. Environmental Science and Technology, 31(2), 321–326.

Guo, H.B., and Barnard, A.S. (2013) Naturally occurring iron oxide nanoparticles: morphology, surface chemistry and environmental stability. Journal of Materials Chemistry A, 1(1), 27–42.

Han, J., and Ro, H.M. (2018) Interpreting competitive adsorption of arsenate and phosphate on nanosized iron (hydr)oxides: Effects of pH and surface loading. Environmental Science and Pollution Research, 25(28), 28572–28582.

Hashem, M.A., Toda, K., and Ohira, S.I. (2015) Leaching behavior of arsenite and arsenate from the contaminated sediment by the effect of phosphate ion under anaerobic conditions. Environmental Earth Sciences, 74(1), 737–743.

He, G.Z., Zhang, M.Y., and Pan, G. (2009) Influence of pH on initial concentration effect of arsenate adsorption on TiO_2 surfaces: Thermodynamic, DFT, and EXAFS interpretations. Journal of Physical Chemistry C, 113(52), 21679–21686.

Henkelman, G., Arnaldsson, A., and Jónsson, H. (2006) A fast and robust algorithm for Bader decomposition of charge density. Computational Materials Science, 36(3), 354–360.

Hiemstra, T. (2013) Surface and mineral structure of ferrihydrite. Geochimica et Cosmochimica Acta, 105, 316–325.

Hingston, F.J., Posner, A.M., and Quirk, J.P. (1971) Competitive adsorption of negatively charged ligands on oxide surfaces. Discussions of the Faraday Society, 52(0), 334–342.

Hu, S., Yan, W., and Duan, J.M. (2015) Polymerization of silicate on TiO_2 and its influence on arsenate adsorption: An ATR-FTIR study. Colloids and Surfaces a-Physicochemical and Engineering Aspects, 469, 180–186.

Hug, S.J. (1997) In situ Fourier transform infrared measurements of sulfate adsorption on hematite in aqueous solutions. Journal of Colloid and Interface Science, 188(2), 415–422.

Jia, Y.F., Xu, L.Y., Wang, X., and Demopoulos, G.P. (2007) Infrared spectroscopic and X-ray diffraction characterization of the nature of adsorbed arsenate on ferrihydrite. Geochimica et Cosmochimica Acta, 71(7), 1643–1654.

Johnston, C.P., and Chrysochoou, M. (2012) Investigation of chromate coordination on ferrihydrite by in situ ATR-FTIR spectroscopy and theoretical frequency calculations. Environmental Science and Technology, 46(11), 5851–5858.

——— (2014) Mechanisms of chromate adsorption on hematite. Geochimica et Cosmochimica Acta, 138, 146–157.

Jonsson, J., and Sherman, D.M. (2008) Sorption of As(III) and As(V) to siderite, green rust (fougerite) and magnetite: Implications for arsenic release in anoxic groundwaters. Chemical Geology, 255(1-2), 173–181.

Kanematsu, M., Young, T.M., Fukushi, K., Green, P.G., and Darby, J.L. (2010) Extended triple layer modeling of arsenate and phosphate adsorption on a goethite-based granular porous adsorbent. Environmental Science and Technology, 44(9), 3388–3394.

Kocourkova-Vikova, E., Loun, J., Sracek, O., Houzar, S., and Filip, J. (2015) Secondary arsenic minerals and arsenic mobility in a historical waste rock pile at Kank near Kutna Hora, Czech Republic. Mineralogy and Petrology, 109(1), 17–33.

Kresse, G., and Furthmuller, J. (1996a) Efficiency of ab-initio total energy calculations for metals and semiconductors using a plane-wave basis set. Computational Materials Science, 6(1), 15–50.

——— (1996b) Efficient iterative schemes for ab initio total-energy calculations using a plane-wave basis set. Physical Review B, 54(16), 11169–11186.

Kresse, G., and Hafner, J. (1993) *Ab initio* molecular-dynamics for liquid-metals. Physical Review B, 47(1), 558–561.

——— (1994) *Ab initio* molecular-dynamics simulation of the liquid-metal–amorphous-semiconductor transition in germanium. Physical Review B, 49(20), 14251–14269.

Kresse, G., and Joubert, D. (1999) From ultrasoft pseudopotentials to the projector

augmented-wave method. Physical Review B, 59(3), 1758–1775.
Krumina, L., Kenney, J.P.L., Loring, J.S., and Persson, P. (2016) Desorption mechanisms of phosphate from ferrihydrite and goethite surfaces. Chemical Geology, 427, 54–64.
Kubicki, J.D., Paul, K.W., Kabalan, L., Zhu, Q., Mrozik, M.K., Aryanpour, M., Pierre-Louis, A.M., and Strongin, D.R. (2012) ATR-FTIR and density functional theory study of the structures, energetics, and vibrational spectra of phosphate adsorbed onto goethite. Langmuir, 28(41), 14573–14587.
Kunhikrishnan, A., Choppala, G., Seshadri, B., Wijesekara, H., Bolan, N.S., Mbene, K., and Kim, W.-I. (2017) Impact of wastewater derived dissolved organic carbon on reduction, mobility, and bioavailability of As(V) and Cr(VI) in contaminated soils. Journal of Environmental Management, 186(2), 183–191.
Liang, X.L., Zhong, Y.H., He, H.P., Yuan, P., Zhu, J.X., Zhu, S.Y., and Jiang, Z. (2012) The application of chromium substituted magnetite as heterogeneous Fenton catalyst for the degradation of aqueous cationic and anionic dyes. Chemical Engineering Journal, 191, 177–184.
Liang, X.L., Zhong, Y.H., Zhu, S.Y., He, H.P., Yuan, P., Zhu, J.X., and Jiang, Z. (2013) The valence and site occupancy of substituting metals in magnetite spinel structure $Fe_{3-x}M_xO_4$ (M = Cr, Mn, Co and Ni) and their influence on thermal stability: An XANES and TG-DSC investigation. Solid State Sciences, 15, 115–122.
Liang, X.L., Wei, G.L., Xiong, J., Tan, F.D., He, H.P., Qu, C.C., Yin, H., Zhu, J.X., Zhu, R.L., Qin, Z.H., and Zhang, J. (2017) Adsorption isotherm, mechanism, and geometry of Pb(II) on magnetites substituted with transition metals. Chemical Geology, 470, 132–140..
Liu, C.H., Chuang, Y.H., Chen, T.Y., Tian, Y., Li, H., Wang, M.K., and Zhang, W. (2015) Mechanism of arsenic adsorption on magnetite nanoparticles from water: Thermodynamic and spectroscopic Studies. Environmental Science and Technology, 49(m13), 7726–7734.
Liu, F., De Cristofaro, A., and Violante, A. (2001) Effect of pH, phosphate and oxalate on the adsorption/desorption of arsenate on/from goethite. Soil Science, 166(3), 197–208.
Livi, K.J.T., Villalobos, M., Leary, R., Varela, M., Barnard, J., Villacis-Garcia, M., Zanella, R., Goodridge, A., and Midgley, P. (2017) Crystal face distributions and surface site densities of two synthetic goethites: Implications for adsorption capacities as a function of particle size. Langmuir, 33(36), 8924–8932.
Loring, J.S., Sandstrom, M.H., Noren, K., and Persson, P. (2009) Rethinking arsenate coordination at the surface of goethite. Chemistry-a European Journal, 15(20), 5063–5072.
Luengo, C., Brigante, M., Antelo, J., and Avena, M. (2006) Kinetics of phosphate adsorption on goethite: Comparing batch adsorption and ATR-IR measurements. Journal of Colloid and Interface Science, 300(2), 511–518.
Lumsdon, D.G., Fraser, A.R., Russell, J.D., and Livesey, N.T. (1984) New infrared band assignments for the arsenate ion adsorbed on synthetic goethite (α-FeOOH). Journal of Soil Science, 35(3), 381–386.
Manning, B.A., and Goldberg, S. (1996) Modeling competitive adsorption of arsenate with phosphate and molybdate on oxide minerals. Soil Science Society of America Journal, 60, 121–131.
Martínez, L., Andrade, R., Birgin, E.G., and Martínez, J.M. (2009) PACKMOL: A package for building initial configurations for molecular dynamics simulations. Journal of Computational Chemistry, 30(13), 2157–2164.
Melamed, R., Jurinak, J.J., and Dudley, L.M. (1995) Effect of adsorbed phosphate on transport of arsenate through an oxisol. Soil Science Society of America Journal, 59(5), 1289–1294.
Mermin, D.N. (1965) Thermal properties of the inhomogeneous electron gas. Physical Review, 137(5A), A1441–A1443.
Mohan, D., and Pittman, C.U. (2007) Arsenic removal from water/wastewater using adsorbents—A critical review. Journal of Hazardous Materials, 142(1-2), 1–53.
Monkhorst, H.J., and Pack, J.D. (1976) Special points for Brillouin-zone integrations. Physical Review B, 13(12), 5188–5192.
Myneni, S.C.B., Traina, S.J., Waychunas, G.A., and Logan, T.J. (1998) Experimental and theoretical vibrational spectroscopic evaluation of arsenate coordination in aqueous solutions, solids, and at mineral-water interfaces. Geochimica et Cosmochimica Acta, 62(19-20), 3285–3300.
Néel, L. (1948) Proprietes Magnetiques Des Ferrites—Ferrimagnetisme Et Antiferromagnetisme. Annales De Physique, 3(2), 137–198.
Neupane, G., Donahoe, R.J., and Arai, Y. (2014) Kinetics of competitive adsorption/desorption of arsenate and phosphate at the ferrihydrite-water interface. Chemical Geology, 368, 31–38.
Noda, I. (1990) Two-dimensional infrared (2D IR) spectroscopy: theory and applications. Applied Spectroscopy, 44(4), 550–561.
Ona-Nguema, G., Morin, G., Juillot, F., Calas, G., and Brown, G.E. (2005) EXAFS analysis of arsenite adsorption onto two-line ferrihydrite, hematite, goethite, and lepidocrocite. Environmental Science and Technology, 39(23), 9147–9155.
O'Reilly, S.E., Strawn, D.G., and Sparks, D.L. (2001) Residence time effects on arsenate adsorption/desorption mechanisms on goethite. Soil Science Society of America Journal, 65(1), 67–77.
Pathak, A.K., and Bandyopadhyay, T. (2016) Solvation of arsenate anion: combined quantum mechanics and molecular dynamics based investigation. Molecular Physics, 114(13), 2029–2036.
Pedersen, H.D., Postma, D., Jakobsen, R., and Larsen, O. (2005) Fast transformation of iron oxyhydroxides by the catalytic action of aqueous Fe(II). Geochimica et Cosmochimica Acta, 69(16), 3967–3977.
Perdew, J.P., Burke, K., and Ernzerhof, M. (1996) Generalized gradient approximation made simple. Physical Review Letters, 77(18), 3865–3868.
——— (1997) Generalized gradient approximation made simple (vol. 77, 3865, 1996). Physical Review Letters, 78(7), 1396. (Erratum)
Peryea, F.J. (1991) Phosphate-induced release of arsenic from soils contaminated with lead arsenate. Soil Science Society of America Journal, 55(5), 1301–1306.
Porezag, D., and Pederson, M.R. (1996) Infrared intensities and Raman-scattering activities within density-functional theory. Physical Review B, 54(11), 7830–7836.
Sabur, M.A., Goldberg, S., Gale, A., Kabengi, N., and Al-Abadleh, H.A. (2015) Temperature-dependent infrared and calorimetric studies on arsenicals adsorption from solution to hematite nanoparticles. Langmuir, 31(9), 2749–2760.
Santos-Carballal, D., Roldan, A., Grau-Crespo, R., and de Leeuw, N.H. (2014) A DFT study of the structures, stabilities and redox behaviour of the major surfaces of magnetite Fe_3O_4. Physical Chemistry Chemical Physics, 16(39), 21,082–21,097.
Santos-Carballal, D., Roldan, A., Dzade, N.Y., and de Leeuw, N.H. (2018) Reactivity of CO_2 on the surfaces of magnetite (Fe_3O_4), greigite (Fe_3S_4) and mackinawite (FeS). Philosophical Transactions of the Royal Society A, Mathematical Physical and Engineering Sciences, 376 (2110).
Sanville, E., Kenny, S.D., Smith, R., and Henkelman, G. (2007) Improved grid-based algorithm for Bader charge allocation. Journal of Computational Chemistry, 28(5), 899-908.
Scott, T.B., Allen, G.C., Heard, P.J., and Randell, M.G. (2005) Reduction of U(VI) to U(IV) on the surface of magnetite. Geochimica et Cosmochimica Acta, 69(24), 5639–5646.
Shannon, R. (1976) Revised effective ionic radii and systematic studies of interatomic distances in halides and chalcogenides. Acta Crystallographica, A32, 751–767.
Sherman, D.M., and Randall, S.R. (2003) Surface complexation of arsenic(V) to iron(III) (hydr)oxides: Structural mechanism from ab initio molecular geometries and EXAFS spectroscopy. Geochimica et Cosmochimica Acta, 67(22), 4223–4230.
Shull, C.G., Wollan, E.O., and Koehler, W.C. (1951) Neutron scattering and polarization by ferromagnetic materials. Physical Review, 84(5), 912–921.
So, H.U., Postma, D., Jakobsen, R., and Larsen, F. (2012) Competitive adsorption of arsenate and phosphate onto calcite; experimental results and modeling with CCM and CD-MUSIC. Geochimica et Cosmochimica Acta, 93, 1–13.
Sprague, D.D., and Vermaire, J.C. (2018) Legacy arsenic pollution of lakes near Cobalt, Ontario, Canada: Arsenic in lake water and sediment remains elevated nearly a century after mining activity has ceased. Water Air and Soil Pollution, 229(3).
Sun, Z.X., Su, F.W., Forsling, W., and Samskog, P.O. (1998) Surface characteristics of magnetite in aqueous suspension. Journal of Colloid and Interface Science, 197(1), 151–159.
Swedlund, P.J., Holtkamp, H., Song, Y.T., and Daughney, C.J. (2014) Arsenate-ferrihydrite systems from minutes to months: A macroscopic and IR spectroscopic study of an elusive equilibrium. Environmental Science and Technology, 48(5), 2759–2765.
Tamura, H., Katayama, N., and Furuichi, R. (1993) Modeling the ion-exchange adsorption of heavy-metal ions on the surface of metal-oxides. Bunseki Kagaku, 42(11), 719–724.
Tang, W., Sanville, E., and Henkelman, G. (2009) A grid-based Bader analysis algorithm without lattice bias. Journal of Physics: Condensed Matter, 21(8), 084204.
Tejedortejedor, M.I., and Anderson, M.A. (1990) Protonation of phosphate on the surface of goethite as studied by cir-FTIR and electrophoretic mobility. Langmuir, 6(3), 602–611.
Tiberg, C., Sjostedt, C., Persson, I., and Gustafsson, J.P. (2013) Phosphate effects on copper(II) and lead(II) sorption to ferrihydrite. Geochimica et Cosmochimica Acta, 120, 140–157.
Villalobos, M., Cheney, M.A., and Alcaraz-Cienfuegos, J. (2009) Goethite surface reactivity: II. A microscopic site-density model that describes its surface area-normalized variability. Journal of Colloid and Interface Science, 336(2), 412–422.
Violante, A., and Pigna, M. (2002) Competitive sorption of arsenate and phosphate on different clay minerals and soils. Soil Science Society of America Journal, 66(6), 1788–1796.
WHO (2011) Guidelines for Drinking-water Quality, 4th ed. World Health Organization.
Winkel, L.H.E., Pham, T.K.T., Vi, M.L., Stengel, C., Amini, M., Nguyen, T.H., Pham, H.V., and Berg, M. (2011) Arsenic pollution of groundwater in Vietnam exacerbated by deep aquifer exploitation for more than a century. Proceedings of the National Academy of Sciences, 108(4), 1246–1251.
Xu, R.K., Kozak, L.M., and Huang, P.M. (2008) Kinetics of phosphate-induced desorption of arsenate adsorbed on crystalline and amorphous aluminum

hydroxides. Soil Science, 173(10), 683–693.
Yan, W., Wang, H.B., and Jing, C.Y. (2016) Adhesion of *Shewanella oneidensis* MR-1 to goethite: A two-dimensional correlation spectroscopic study. Environmental Science and Technology, 50(8), 4343–4349.
Zhang, M.Y., Pan, G., Zhao, D.Y., and He, G.Z. (2011) XAFS study of starch-stabilized magnetite nanoparticles and surface speciation of arsenate. Environmental Pollution, 159(12), 3509–3514.
Zhang, J.H., Zhang, C.H., Wei, G.L., Li, Y., Liang, X.L., Chu, W., He, H.P., Huang, D.Y., Zhu, J.X., and Zhu, R.L. (2017a) Reduction removal of hexavalent chromium by zinc-substituted magnetite coupled with aqueous Fe(II) at neutral pH value. Journal of Colloid and Interface Science, 500, 20–29.
Zhang, L., Qin, X., Tang, J., Liu, W., and Yang, H. (2017b) Review of arsenic geochemical characteristics and its significance on arsenic pollution studies in karst groundwater, Southwest China. Applied Geochemistry, 77, 80–88.
Zhao, H.S., and Stanforth, R. (2001) Competitive adsorption of phosphate and arsenate on goethite. Environmental Science and Technology, 35(24), 4753–4757.
Zhao, L.J., Zhang, H.J., Xing, Y., Song, S.Y., Yu, S.Y., Shi, W.D., Guo, X.M., Yang, H.H., Le, Y.Q., and Cao, F. (2008) Morphology-controlled synthesis of magnetites with nanoporous structures and excellent magnetic properties. Chemistry of Materials, 20(1), 198–204.

Manuscript received October 31, 2019
Manuscript accepted July 6, 2020
Manuscript handled by Andrew Madden

Endnote:

[1]Deposit item AM-21-37350, Online Material. Deposit items are free to all readers and found on the MSA website, via the specific issue's Table of Contents (go to http://www.minsocam.org/MSA/AmMin/TOC/2021/Mar2021_data/Mar2021_data.html).